

The EUV Late-Phase: Statistical Results from 15 Years of Solar Dynamics Observatory Observations

Harry J. Grotorex¹, Aisling N. O'Hare¹, Susanna Bekker¹,
Ryan J. Campbell¹, Daniel C. Keane², and Ryan O. Milligan¹

¹ Astrophysics Research Centre, School of Mathematics and Physics, Queen's
University Belfast, Belfast, United Kingdom, BT7 1NN

² School of Physics and Astronomy, University of Glasgow, Glasgow, United
Kingdom, G12 8QQ

December 24, 2025

Abstract

Since its launch in 2010, the *Solar Dynamics Observatory* (SDO) has provided continuous, high-cadence, multi-wavelength observations of the Sun, capturing thousands of solar flares and offering new insights into coronal dynamics. Among the discoveries enabled by SDO is the EUV late-phase (ELP), characterised by a secondary enhancement in warm coronal emission occurring tens of minutes after the main flare. While recent work has demonstrated the relevance of the ELP for space weather, the statistical behaviours and physical origins are not fully understood. Here, we present the most comprehensive statistical analysis of the ELP to date, based on 15-years of Fe xvi (335 Å) observations from the *Atmospheric Imaging Assembly* onboard SDO (SDO/AIA). From a sample of 5335 isolated flares between 2010 and 2025, we identify and validate 467 ELP events. The overall ELP occurrence rate was found to be 8 %, with no significant dependence on the solar cycle and only a modest enhancement in the low-mid M-class range. The ELP typically exhibited an onset delay of 19 minutes, a peak-to-peak delay of 88 minutes, and a duration of 93 minutes. Strong correlations were found between ELP rise and decay rates ($\rho = 0.76$), and between flare and ELP impulsivity ($\rho = 0.61$). However, a comprehensive pairwise analysis revealed no significant correlation between the flare and ELP phases ($|\rho| < 0.3$). A Principal Component Analysis of flare and ELP properties revealed three dominant axes of variation, corresponding to a timescale component, an energy-release intensity axis, and a partitioning of energy between the

*Corresponding author: h.grotorex@qub.ac.uk

flare and the ELP, suggesting that ELP evolution is governed by both flare loop properties and reconnection-driven energetics, likely modulated by a finite magnetic energy budget. These results highlight the continuing importance of SDO’s long-term, high-resolution observations for uncovering new aspects of solar flare evolution and improving understanding of the Sun-Earth connection.

1 Introduction

Since its launch in February 2010, the Solar Dynamics Observatory (SDO; Pennell et al. 2012) has provided continuous, high-cadence imaging and spectroscopic coverage of extreme ultraviolet (EUV) emission from the solar atmosphere, revealing the complex dynamics of the solar atmosphere. In the standard model of solar flares (CSHKP; Carmichael 1964, Sturrock 1966, Hirayama 1974, Kopp and Pneuman 1976), the reconnection of opposing polarity coronal magnetic fields releases stored magnetic free-energy, accelerating charged particles along newly formed closed loops, which deposit energy in the chromosphere through Coulomb collisions with dense plasma at the loop footpoints [Aschwanden, 2002, Holman et al., 2011]. The resulting energy deposition drives rapid heating to temperatures exceeding 10^7 K and the explosive expansion of chromospheric plasma into the overlying coronal loops with upflow velocities of several hundred km s^{-1} (Chromospheric Evaporation; Fisher et al. 1985, Milligan et al. 2006, del Zanna et al. 2006, Milligan and Dennis 2009, Tian et al. 2015, Reep et al. 2016), which subsequently radiates in the soft X-ray (SXR) regime.

Flare evolution can be divided spectrally, spatially, and temporally into a series of phases. The preflare phase marks the accumulation of magnetic free-energy and is occasionally accompanied by hot onsets, which are instances of localised high-temperature emission preceding the impulsive rise [Hudson, 1991, Simoes et al., 2015, Hudson et al., 2021]. The impulsive phase corresponds to the rapid release of energy, producing intense nonthermal bremsstrahlung hard X-rays (HXRs) and chromospheric EUV emission emanating from the region surrounding the footpoints at the base of the flare loops. This is followed by the gradual phase, characterised by the dominance of SXR emission from hot flare loops. In accordance with the Neupert effect [Neupert, 1968], the impulsive phase HXR flux approximates the time derivative of the gradual phase SXR flux, with the observed delay between the two peaks reflecting the timescale of chromospheric evaporation. Temperatures within flaring loops can exceed 10–20 MK, in contrast to the ambient corona (1–3 MK). Subsequent loop cooling has been found to occur initially via thermal conduction, followed by radiative cooling as the temperature drops to EUV emitting temperatures [Klimchuk, 2006, Raftery et al., 2009]. As cooling progresses, high-temperature EUV lines diminish and cooler lines become more prominent.

Extending beyond the main phase, the EUV late-phase (ELP) refers to a secondary peak of warm coronal emission, such as Fe XV and Fe XVI, occurring

several minutes to a few hours after the initial solar flare [Woods et al., 2011, Woods, 2014]. The ELP is empirically defined by several key characteristics first outlined by Woods et al. [2011]: (1) a delayed secondary peak in warm coronal EUV irradiance occurring tens of minutes to hours after the GOES SXR maximum; (2) the absence of a corresponding second enhancement in SXRs or in hot flare lines, such as Fe XX and Fe XXIII; (3) an association with an eruptive event such as a coronal mass ejection or coronal dimming; and (4) spatially distinct emission from a separate system of large, high-altitude loops that brighten well after the main flare arcade.

The discovery of the ELP early in the SDO era raised fundamental questions surrounding the transport of energy in the solar atmosphere post-flare, yet relatively few studies have examined the physical origin of this emission. Two prevailing theories have been proposed. The first attributes ELP emission to the cooling of large, overlying coronal loops that were heated during the main phase of the flare, with their long cooling times reflecting the large spatial extent of these loops [Hock et al., 2012, Dai and Ding, 2018, Zhong et al., 2021]. The second suggests that the ELP results from continued magnetic reconnection during the decay phase of the flare, with smaller energy releases generating renewed emission in warm EUV wavelengths [Sun et al., 2013, Dai et al., 2013]. These two scenarios are not mutually exclusive, and evidence for both processes operating within the same active region has been observed [Zhou et al., 2019].

Not all flares possess an ELP; Woods et al. [2011] found the phenomenon to occur in 14 % of solar flares, with a greater probability for events of higher magnitude. A further study by Woods [2014] found that ELP flares occur in a consistently higher proportion before and after solar maximum than during it, when using dual-decay events in SXRs as a proxy for ELP. More recently, a statistical analysis of ~ 1800 disk-integrated flare observations from the *Extreme-Ultraviolet Variability Experiment* (EVE; Woods et al. 2012) instrument onboard SDO by Ornić et al. [2025], found that approximately 10 % of flares exhibited a late-phase, and that most were classified as extreme ELP flares, where the flux of warm coronal emission in the late-phase exceeded that in the main phase [Liu et al., 2015].

It is well established that both EUV and SXR emissions from solar flares have a measurable impact on the Earth’s ionosphere. The altitude at which this radiation is effective depends on several factors, including the wavelength of the emission. Higher energy photons penetrate deeper into the atmosphere, so enhancements in SXR flux during solar flares primarily affect the lower ionosphere (D-region) and are routinely identified through perturbations in Very Low Frequency (VLF) radio signals [Pant, 1993, McRae and Thomson, 2004, Raulin et al., 2013, Hayes et al., 2021, Bekker and Korsunskaya, 2023]. At higher altitudes, within the E- and F-regions, increases in ionospheric electron density, which are predominantly driven by EUV flare emission at wavelengths shortward of 350 Å [Mitra, 1974, Leonovich et al., 2002, Zhang et al., 2011, Watanabe et al., 2021, Solomon and Qian, 2005], are observed in total electron content (TEC) measurements derived from the Global Navigation Satellite System (GNSS). The Fe XV and Fe XVI lines that characterise the ELP are known

to be geoeffective and therefore represent a key source of delayed ionospheric heating. Recent work by Liu et al. [2024] and Bekker et al. [2024], Bekker et al. [2025] demonstrated that ELP emission can produce a measurable enhancement in TEC, with the latter finding that the ionospheric response associated with the ELP can even exceed the ionospheric effect of the main phase of an X-class flare, particularly if the flare occurs near the solar limb, where significant attenuation of the cold chromospheric lines, which ionise the ionosphere during the impulsive phase, is usually observed. These findings highlight that the EUV late-phase can contribute significantly to the total flare energy deposited into the upper atmosphere. Understanding the temporal behaviour, occurrence frequency, and physical drivers of ELP emission is therefore essential for improving models of ionospheric variability and for advancing space weather forecasting capability.

Despite the apparent importance of the ELP for space weather, there remain relatively few studies of this phenomenon, which may partly reflect its inherent rarity. Since the discovery works by Woods et al. [2011] and Woods [2014], SDO has captured thousands of additional flares. However, following the loss of the higher-energy MEGS-A channel of the *Multiple EUV Grating Spectrograph* (MEGS) on the EVE instrument in 2014, continuous full-disk spectral measurements across the 50-370 Å range were no longer available. While the MEGS-B channel coverage was subsequently extended down to approximately 330 Å, EVE currently operates on a flare trigger system with a limited duty cycle. This trigger is initiated when the EUV flux measured by the *Extreme Ultraviolet Spectrophotometer* (ESP; Didkovsky et al. 2012) exceeds levels approximately equal to those associated with an M1.0 class flare. This flare-triggered mode will not capture smaller C-class flares and is not guaranteed to capture the full evolution or the extended timescales of the late-phase. Consequently, it is not feasible to perform a comprehensive long-term statistical study of ELP occurrence using SDO/EVE data alone. This limitation presents a unique opportunity to apply similar techniques to spatially-resolved imaging from the *Atmospheric Imaging Assembly* (AIA; Lemen et al. 2011, Boerner et al. 2012), which has observed several of the key ELP wavelengths identified by Woods et al. [2011] with continuous full-disk coverage since 2010.

Here we present a comprehensive analysis of more than 5000 isolated solar flares observed by SDO/AIA between 2010 and 2025, providing partial coverage of two solar cycles. This approach overcomes the limitations of previous studies, allowing us to examine the long-term behaviour of the ELP and to investigate potential solar cycle dependencies. The use of spatially-resolved measurements removes the ambiguity inherent in disk-integrated irradiance data, enabling us to directly characterise late-phase emission from individual flare regions. We also perform a comparative analysis between SDO/EVE and SDO/AIA detections from 2010–2014 to quantify the impact of instrument choice on measured ELP occurrence and to assess the extent to which disk-integrated observations may overestimate or misidentify late-phase events. Our approach focusses on the warm coronal Fe XVI (335 Å) emission, which is known to be geoeffective [Bekker et al., 2024]. We derive observational metrics that describe the general behaviour

of Fe XVI ELP emission, quantify its occurrence rate, class dependence, and solar cycle variation, and explore the relationships between main phase and late-phase emission characteristics. Particular attention is given to parameters that directly influence the ionosphere, such as impulsivity, onset delays, and decay times. Together, these analyses establish Fe XVI as a focal diagnostic of the EUV late-phase, providing a comprehensive, long-term characterisation of its behaviour. The results form a foundation for future investigations into the space weather impacts of late-phase emission and offer a framework for targeted analyses of the phenomenon. The observational data, event selection criteria, processing methods, and procedures used for ELP detection, validation, and the derivation of temporal and morphological parameters are described in Section 2. The statistical results, including occurrence rates, solar cycle variation, temporal relationships, and impulsivity analysis, are presented in Section 3. A discussion of these findings in the context of previous work and potential space weather implications is given in Section 4. Finally, the main conclusions are summarised in Section 5.

2 Observations and Methods

The following section outlines the data selection and analysis techniques used in this study, including the construction of the flare sample, processing of observation data, ELP identification methods, and the characteristic metrics calculated for validated ELP events.

2.1 Flare Sample and Definition

To conduct a precise and comprehensive examination of the EUV late-phase, a sample of isolated solar flares was required that covered the operational lifetime of SDO to date. To be considered isolated, each flare was required to have no preceding events within 1 hour and no additional events for at least 3 hours after its end time, where these timings were defined by the SXR observations from the *X-ray Sensor* (XRS; Hanser and Sellers 1996) on board the primary *Geostationary Environmental Operational Satellite* (GOES) spacecraft. This isolation criterion ensured that any detected ELP signature was unambiguous and that a suitable background period could be identified for subtraction and normalisation of EUV fluxes, allowing for accurate determination of ELP presence. In addition, each flare was required to be of magnitude C1.0 or greater (as determined by the peak flux in the 1–8 Å GOES/XRS measurements) to aid the identification and distinction of flare and ELP signatures. From the GOES flare list, approximately 5500 isolated events were identified between 2010–2025. Examination of the SXR timeseries for each GOES flare revealed a number of events unsuitable for analysis due to data dropouts, transmission gaps, or anomalies within the isolation window. Additional events were removed due to missing or corrupted data in the EUV channels. Excluding these cases yielded a final sample of 5335 flares for subsequent analysis.

Table 1: Summary of the selected EUV channels from AIA, including the Full Width at Half Maximum (FWHM) of the imaging channel, the dominant emission species/constituent in that channel, the source region in the solar atmosphere, and the approximate emission temperature as a logarithm. Table adapted from Lemen et al. [2011].

Channel (Å)	FWHM ($\Delta\text{Å}$)	Constituent	Region	$\log(T)$
131	4.4	Fe xx, Fe xxiii	Flaring Corona	7.0, 7.2
171	4.7	Fe ix	QS Corona and Upper-TR	5.8
304	12.7	He ii	Chromosphere and TR	4.7
335	16.5	Fe xvi	Coronal Active Regions	6.4

2.2 Data Acquisition and Processing

Flare locations were obtained from the Heliophysics Event Knowledgebase (HEK; Hurlburt et al. 2012) in helioprojective coordinates. For each flare, L 1.5 AIA image data were accessed through the *Joint Science Operations Center* (JSOC) using 500×500 arcsec cutouts centred on the flare coordinates. Each dataset covered a 6 hour window to capture both the impulsive and gradual evolution of the flare and to monitor any subsequent ELP activity. The data were sampled at 60 s cadence across four EUV wavelengths: 131 Å, 171 Å, 304 Å, and 335 Å. These wavelengths sample emissions across a broad range of plasma temperatures and mirror the methods of Woods et al. [2011]. The 131 Å channel is dominated by hot coronal lines (Fe xx, Fe xxiii), 171 Å traces cooler coronal emission (Fe ix), 304 Å samples the chromospheric and transition region response (He ii), and 335 Å captures warm coronal emission (Fe xvi) that is present in the EUV late-phase. A summary of these channels is provided in Table 1.

For each event, the flux in each 60 s AIA cutout was integrated over the full field of view to yield a single total flux value per image, in Data Numbers (DNs), for each wavelength. These measurements were used to construct EUV flux timeseries spanning a 6 hour window centred on the GOES flare time. To isolate flare- and late-phase-related enhancements, a background subtraction was performed using a one-hour preflare interval. This interval was chosen to ensure a sufficiently long and stable background baseline while avoiding contamination from earlier activity. A low-order polynomial (typically second or third order) was fit to this preflare segment to capture any slow-varying background trends, such as instrumental drift or gradual evolution in active region brightness. This fitted background was then extrapolated across the full 6 hour window and subtracted from the original timeseries. The result was then normalised to the preflare background level to express all flux enhancements as relative changes above quiescent conditions. To further reduce noise while preserving genuine flare-related structure, a Savitzky-Golay filter [Savitzky and Golay, 1964] was applied using a third-order polynomial and a smoothing window of approximately 10 minutes. The resulting normalised fluxes were combined with the corresponding SXR timeseries from GOES to form the basis for ELP

identification.

2.3 ELP Detection and Validation

To identify the presence of ELPs in the flare sample, a manual inspection of the combined timeseries was performed, with a specific focus on the Fe XVI emission. A set of primary detection criteria were defined that were congruent with the first and second criteria outlined by Woods et al. [2011] for SDO/EVE observations but adapted to fit the aims of this analysis. The criteria for a positive initial ELP detection were as follows:

1. All positive ELP cases must have a distinct secondary peak in the 335 Å channel flux that occurs after the initial flare event with no co-temporal increase in the SXR flux or the other EUV wavelengths.
2. A clearly identifiable minimum point must exist in the 335 Å flux between the flare end and ELP onset for all positive cases. However, we do not require the time delay between the flare end and ELP start to exceed a minimum threshold as this is a metric we intend to measure.
3. The magnitude of the secondary peak must be greater than 10 % of the initial flare peak in 335 Å. This threshold is lower than that adopted by Ornig et al. [2025]; however, the typical short term variability of the background-subtracted Fe XVI flux in our smoothed AIA lightcurves is only a few percent, so a 10 % enhancement represents a clear, statistically significant deviation above both the preflare background and instrumental noise. Given the space weather implications of ELP emission, where even small changes in EUV flux can have a detectable impact on the ionosphere [O’Hare et al., 2025], this smaller threshold was considered sufficient.

Consistent with other statistical investigations of the ELP [Woods, 2014, Chen et al., 2020, Ornig et al., 2025], the requirement that the flare be eruptive (criterion 3 of Woods et al. 2011) was neglected, as this condition is not essential for identifying potentially geoeffective ELP emission and would introduce unnecessary complexity for a dataset of this scale. For each candidate, the flare and ELP start, peak, and end times were determined directly from the Fe XVI lightcurves. The flare start time was defined as the first sustained rise in Fe XVI exceeding a few percent above the preflare background for at least three consecutive 60 s bins. The flare peak time was defined as the point at which the initial Fe XVI increase reached its maximum value. The flare end time was defined as the point at which the initial Fe XVI emission decayed to approximately 50 % of its maximum value. The ELP onset corresponded to the turning point following the flare decay where the Fe XVI emission began a renewed increase. Similar to the flare, the ELP peak time corresponded to the time of maximum Fe XVI flux thereafter, and the ELP end time corresponded to the point at which the Fe XVI flux had decayed to 50 % of its late-phase peak value. While this requirement of a 50 % decay is not necessarily physically prescriptive, it provides a consistent,

reproducible metric across the full sample and allows direct comparison between both phases. An example of a combined EUV and SXR timeseries for a positive ELP identification is presented in Figure 1.

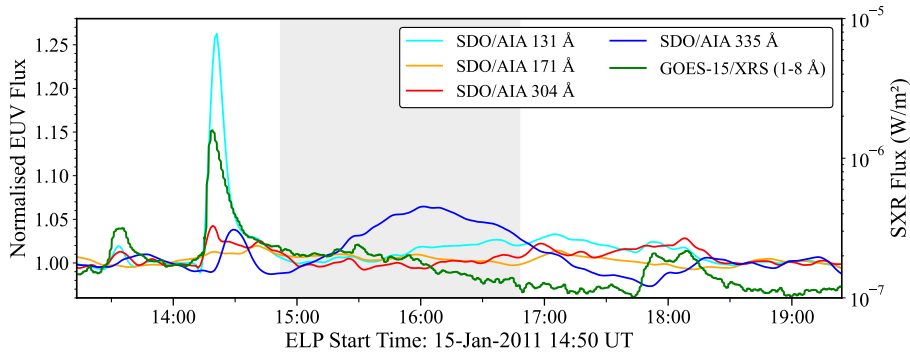


Figure 1: Example of a combined EUV and SXR timeseries for a C1.1 flare corresponding to a positive ELP identification. Each EUV line was derived from integrated SDO/AIA cutout data. From the Fe XVI line (blue), two clear peaks are resolvable corresponding to the flare and ELP, respectively. The grey shaded represents the derived ELP period based on the characteristics outlined in Section 2.3

Flares meeting these conditions were labelled as ELP candidates. Each candidate was then subjected to a validation stage corresponding to the fourth criterion of Woods et al. [2011], requiring that the ELP emission originate from a spatially distinct loop system. AIA 335 Å images at the flare and ELP peak times were compared manually, along with a difference image of the two. Valid ELP events exhibited clearly separated emission structures, with the late-phase loops overlying or adjacent to the main flare loop system. An example of two clearly distinct emission regions corresponding to the flare and ELP event in the same active region is presented in Figure 2. Here, the two brightenings originate from clearly separate loop systems, with the late-phase arcade appearing at higher altitude and displaced relative to the main flare loops. Cases lacking distinct spatial separation or displaying only diffuse post-flare brightening were rejected as misidentifications. In practice, these ambiguous detections typically occurred in weak events with marginal ELP flux enhancements or in large, fragmented active regions.

2.4 Analysis of ELP Characteristics

Following identification and validation of the ELP events, a series of quantitative parameters were calculated to describe their behaviour. These metrics were designed to capture the key physical properties of both the flare and late-phase, and to allow assessment of their potential space weather relevance. All

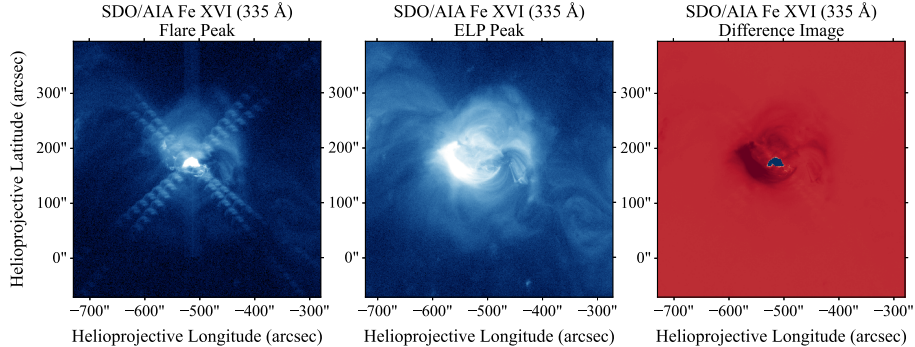


Figure 2: Example of the spatial distinction between the main flare and the ELP emission in SDO/AIA Fe XVI (335 Å) images. The left and middle panels show the 500×500 arcsec AIA cutouts at the flare peak and the ELP peak, respectively. The right panel shows the difference image (ELP peak minus flare peak), where the dark region highlights the location of the enhanced late-phase emission, distinct from the brighter main phase region (blue).

times were defined in Fe XVI, providing a consistent diagnostic of warm coronal emission independent of GOES SXR timings. The start, peak, and end times of both the flare and ELP were used to derive a set of temporal parameters. These included the onset delay (the interval between the end of the flare and the start of the ELP), the peak delay (the interval between the flare and ELP maxima), and the respective rise, decay, and total durations of each phase. To describe the temporal morphology of the ELP lightcurve, a skew parameter was defined as the ratio of the rise time to the decay time, where values greater than unity indicate a more impulsive rise and slower decay. To further characterise the late-phase evolution, rise and decay rates were also calculated from the Fe XVI lightcurves. The rise rate was defined as the flux-change per unit time between the ELP start and peak, and the decay rate as the corresponding flux-change between the ELP peak and end.

In addition, the relative enhancement of Fe XVI emission for each phase was calculated as the ratio of the peak flux to the fitted preflare background ($F_{\text{peak}}/F_{\text{bg}}$), providing a measure of the fractional brightening above the local background. The impulsivity of each phase was calculated following the definition of Tamburri et al. [2024], adapted here for Fe XVI emission as:

$$I = \frac{(F_{\text{peak}} - F_{\text{start}})/F_{\text{bg}}}{(t_{\text{peak}} - t_{\text{start}})} \quad (1)$$

The global averages reported in this study are accompanied by the standard deviation (σ) of each parameter across the full ELP sample. These values reflect the intrinsic variability of the population rather than representing formal measurement uncertainties. Timing precision is constrained to the selected 60 s cadence of the AIA data, introducing an uncertainty of approximately ± 30 s in

start and peak times. Flux-related metrics inherit this temporal uncertainty and an additional few percent variability from instrumental noise and background normalisation. These uncertainties are small compared with the overall spread of the measured distributions and do not affect the statistical trends discussed in the following section.

To test for relationships among the timing and morphological parameters, a pairwise correlation analysis was performed on all validated ELP events. The variables included the flare and ELP durations, onset and peak delays, ELP rise and decay times, and the skew parameter. For each parameter pair, the Spearman (ρ ; Spearman 1904) correlation coefficients were computed, with uncertainties estimated through a 1000-sample bootstrap procedure that provided 1σ confidence intervals for each coefficient. The resulting correlation matrices were examined to identify statistically significant and physically meaningful trends among the derived parameters. To explore broader structure among the measured flare and ELP parameters, a principal component analysis (PCA; Jolliffe 2011) was also performed on the events with confirmed ELP. Thirteen variables, derived from the above analysis steps, spanning timescales, impulsivities, radiative enhancements, and rates were included. Each variable was standardised prior to decomposition to prevent scale-driven bias. The first three principal components were then retained and used to assess dominant modes of variability across the sample.

3 Results

The following section presents the results of a statistical analysis of the validated ELP events. We first describe their overall occurrence and dependence on flare magnitude and solar cycle phase, before comparing detection statistics between SDO/AIA and SDO/EVE. We then examine the temporal, morphological, and flux-related characteristics of the ELP derived from the Fe XVI metrics defined in Section 2.

3.1 ELP Occurrence Rates

From examination of the AIA timeseries for the 5335 total flares in the sample, 515 events (9.65 %) were initially classified as potential ELP flares. Following a manual examination of the associated 335 Å images, 467 events were confirmed as ELPs (8.75 %). In terms of flare magnitude, ELPs were detected in 6.99 % of C-class, 19.32 % of M-class, and 19.18 % of X-class flares, indicating a preference towards moderate-to-large events. However, the proportions for higher magnitude flares are subject to larger statistical uncertainty due to their smaller sample sizes. Table 2 summarises the detection statistics for each GOES class.

To further assess the class dependence of ELP emission, GOES classes were subdivided into finer class bins. Figure 3 shows the ELP fraction as a function of flare magnitude. The occurrence rate increased from 6.2 % for C1.0–C2.9 events to a maximum of 27.2 % for M3.0–M5.9 events before decreasing at

Table 2: Summary of ELP occurrence rates by GOES class. The number of total flares (N), detected ELPs ($ELP_{\text{Potential}}$), and validated ELPs (ELP_{True}) are listed, together with the corresponding percentages.

GOES Class	N	$ELP_{\text{Potential}}$	ELP_{True}	ELP%
C	4580	361	320	6.99
M	678	138	131	19.32
X	73	14	14	19.18
Overall	5335	515	467	8.75

higher magnitudes. A secondary rise is observed among low-to-moderate X-class flares; however, the reduced number of events in these categories introduces substantial statistical uncertainty. The error bars in Figure 3 represent 95 % Wilson binomial confidence intervals, which provide a more accurate measure of proportional uncertainty for finite sample sizes than the standard normal approximation [Wilson, 1927].

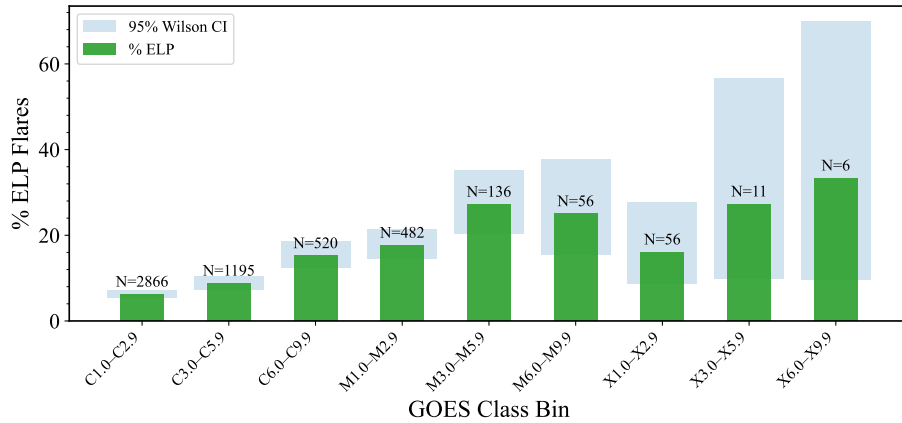


Figure 3: Percentage of events with an associated ELP by GOES class bin. Error bars denote 95 % Wilson binomial confidence intervals. The annotated N-values correspond to the total number of flares from the full sample of 5335 flares.

To investigate the long-term variability of ELP occurrence, the validated ELP sample was examined across the 15 year period covered by the dataset. The monthly mean sunspot number was used as a proxy for global solar activity and to define the phase of the solar cycle. The temporal variation in ELP occurrence was evaluated by computing the total number of validated ELP detections per month, the total number of flares observed, and the fraction of these flares exhibiting an ELP. Figure 4 presents the comparative evolution of solar activity and ELP occurrence, smoothed using a six-month running mean to emphasise large-scale trends and minimise short-term fluctuations.

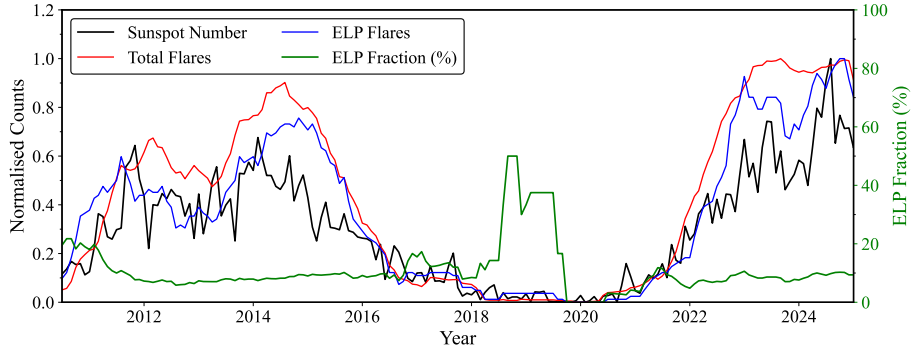


Figure 4: Temporal variation of ELP occurrence from 2010 to 2025. The black line indicates the six-month smoothed monthly mean sunspot number used as a proxy for solar activity level and therefore solar cycle. The red line denotes the total number of flares per month, and the blue line shows the number of validated ELP detections in that month. The percentage of ELPs detected in each month (normalised to the total number of flares) is shown in green.

Figure 4 demonstrates that there is no strong solar cycle dependence in the occurrence of ELPs. The solar cycle trend is clearly evident in the sunspot number, with activity levels rising and falling periodically and an approximate 11 year interval between successive peaks. The total flare count and the number of ELP detections track the changing global activity level, as indicated by the coherence between the black, red, and blue curves. The fraction of ELP events remains relatively uniform across the 15-year period, with an average value of $\sim 10\%$, consistent with the overall occurrence rate reported above. A local enhancement in the ELP fraction between 2018 and 2020 coincides with solar minimum; however, this feature occurs during a period of low flare numbers (47 isolated flares) and is therefore subject to statistical uncertainty. A larger flare sample during this epoch would be required to confirm whether this increase is significant.

3.2 Cross-comparison of SDO/AIA and SDO/EVE

To assess the instrumental impact on ELP identification, a comparison was performed between detections from SDO/AIA and SDO/EVE over the period of 2010–2014. This window covers the period during which the MEGS-A component of EVE was fully operational. These measurements are required here as the MEGS-A spectral range encapsulates all wavelengths examined for the ELP identification from AIA, allowing for a direct comparison of ELP detection capabilities using each instrument. All flares from the AIA sample with complete EVE coverage during this period were identified, yielding more than 500 events. A representative subsample of 500 flares was selected for analysis, comprising of approximately 86 % C-class, 12 % M-class, and 2 % X-class events, thus main-

taining a proportional class representation while reducing the computational demand of the comparison.

For the EVE analysis, Level 2B spectral line data at 60 s cadence were used to construct lightcurves with identical wavelengths to those in the AIA analysis and analysed over the same six hour windows. Background subtraction, normalisation, and smoothing were applied identically to those used for the AIA data to ensure consistency between the two datasets. The same ELP detection criteria described in Section 2.3 were then applied to the EVE lightcurves.

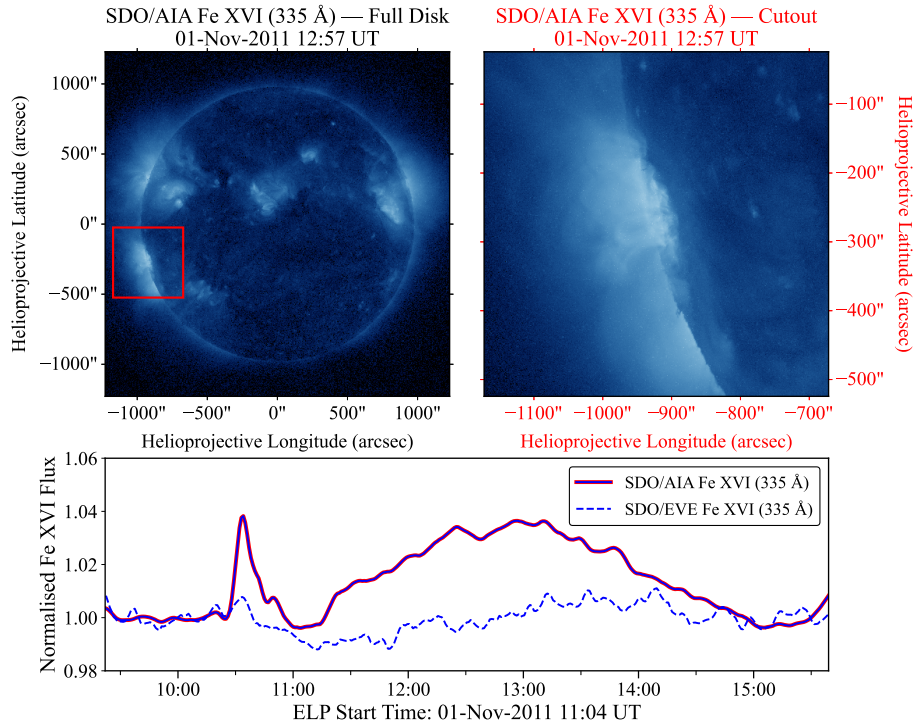


Figure 5: Comparison between SDO/AIA and SDO/EVE observations of the Fe XVI emission for a representative ELP event. Top Left: Full-disk AIA 335 Å image at the ELP peak time. The red box denotes the 500×500 arcsec cutout region corresponding to the ELP/flare site used as a proxy for the effective field of view of the disk-integrated EVE measurements. Top right: AIA 335 Å cutout image of the region enclosed by the red box in the full-disk image. Bottom: Normalised Fe XVI lightcurves from AIA (blue-red line) and EVE (blue dashed line) for the same event. The ELP signal is clearly visible in the spatially-resolved AIA data but not in the disk-integrated EVE irradiance.

Across the 500 flares examined, the classifications derived from EVE and AIA agreed in approximately 80 % of cases. This agreement demonstrates broad consistency between the instruments but also highlights the potential

discrepancies presented by using different measurements to identify ELPs. The spatially integrated nature of EVE means that emission from multiple active regions contributes to the total irradiance, which can obscure the Fe XVI emission associated with the ELP. Additionally, the associated background flux for disk-integrated measurements may be elevated by multiple active regions, potentially masking smaller ELP events. These effects lead to potential misidentification of the ELP, particularly during periods of high solar activity. Figure 5 exemplifies this, with the upper-left panel demonstrating a full-disk AIA image in 335 Å of the Sun at the point of maximum ELP emission associated with a flare. This image represents the effective field-of-view (FOV) for the EVE instruments disk-integrated measurements. The image shows several active regions present on the disk and limb, with the red bounding box representing the subsequent AIA cutout region centred around the ELP active region analogous to those used for ELP identification in this study. The upper-right panel contains a 500×500 arcsec AIA cutout image centered around the flare location. The bottom panel compares the AIA and corresponding EVE timeseries, where the dashed line corresponds to the disk-integrated irradiance from EVE, and the solid line denotes the derived timeseries from the AIA cutouts, each normalised to their respective background as described in Section 2.3. From these plots, it is clear that the enhancement in the EVE signal is diminished compared to that from AIA and thus no clear ELP can be detected from these observations. On the other hand, a clear ELP signal is identifiable in the spatially constrained AIA data.

While the example shown in Figure 5 illustrates an ELP identified in AIA but not EVE, the inverse case also occurred in a small subset of events. These instances likely arise when the AIA cutout FOV does not fully capture the spatial extent of the ELP emission, particularly for eruptive flares involving large-scale displacements or for active regions dispersed across the disk (Figure 6). Additionally, coincident emission from multiple regions contributing to the EVE signal, but outside the AIA bounding box, may produce apparent late-phase signatures in EVE that are not visible in the AIA FOV. These alternative scenarios are discussed further in Section 4. For now, we affirm that the AIA results provide a more robust estimate of ELP occurrence.

3.3 Temporal Properties of ELP Emission

To characterise the evolution of the ELP, all timing analyses were performed using the Fe XVI lightcurves from AIA. The parameters examined here are related to the relative timing and duration of the ELP emission with respect to the main flare exclusively in Fe XVI. Table 3 contains a summary of the derived parameters, which are further discussed in Sections 3.3.1–3.3.4.

3.3.1 ELP Onset Delay

Here, the onset delay (Δt_{onset}) refers to the duration between the end of the Fe XVI emission from the main flare and the start of the Fe XVI emission associ-

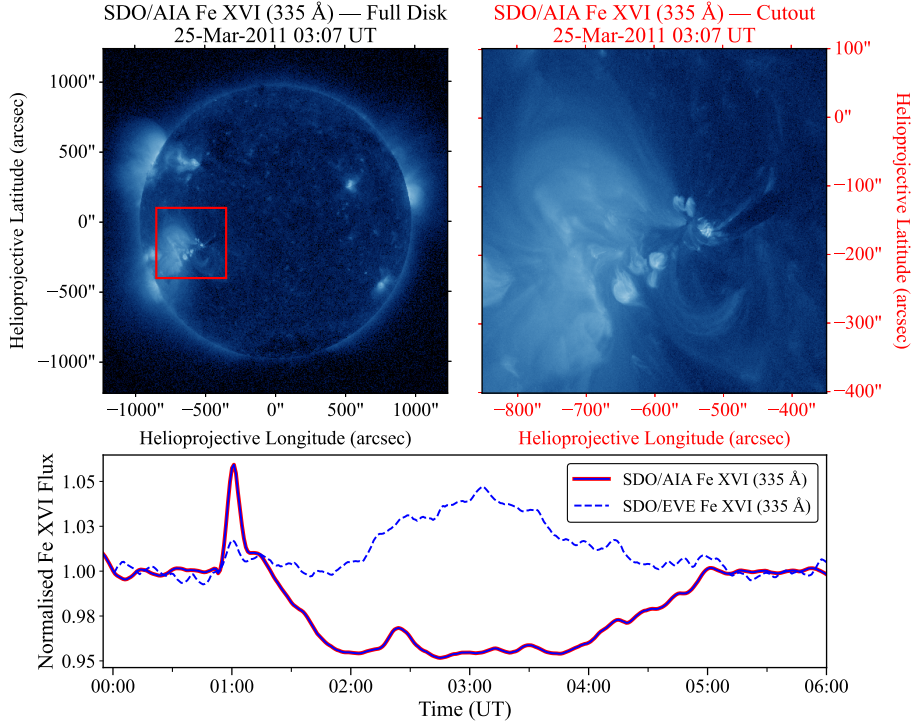


Figure 6: Comparison between SDO/AIA and SDO/EVE observations of the Fe XVI emission for a representative ELP event. Top Left: Full-disk AIA 335 Å image at the ELP peak time. The red box denotes the 500×500 arcsec cutout region corresponding to the ELP/flare site used as a proxy for the effective field of view of the disk-integrated EVE measurements. Top right: AIA 335 Å cutout image of the region enclosed by the red box in the full-disk image. Bottom: Normalised Fe XVI lightcurves from AIA (blue-red line) and EVE (blue dashed line) for the same event. An ELP signal is visible in the disk-integrated EVE irradiance but the spatially-resolved AIA data demonstrates a dip with no signal, potentially associated with an absence of emitting material due to the initial flare eruption.

ated with the corresponding ELP. Figure 7 presents a histogram of onset delay times for the 467 validated ELP events in the sample. The mean onset delay is 19 ± 18 minutes, with a median value of 13 minutes. The large spread reflects the intrinsic variability of this parameter, with most events exhibiting short delays of less than 20 minutes, while a smaller number show significantly longer separations. Beyond $\Delta t_{\text{onset}} > 30$ minutes, the frequency decreases rapidly, with fewer than 20 events in each successive 10 minute bin. The onset delay between flare-related and ELP-related Fe XVI emission is highly variable but typically remains within the first 20 minutes following the main phase of the

Table 3: Summary of temporal parameters derived from the observed Fe XVI emission for the 467 validated ELP events examined in this study. Uncertainties represent the standard deviation (σ) of each quantity across the sample. Each parameter is analysed in detail in their related subsections.

Parameter	Mean $\pm \sigma$	Median $\pm \sigma$	Min	Max
Onset Delay (min)	19 \pm 18	13 \pm 5	2	119
Peak-to-Peak Delay (min)	88 \pm 41	82 \pm 10	8	226
Flare Duration (min)	23 \pm 11	20 \pm 6	4	61
ELP Duration (min)	93 \pm 42	89 \pm 15	15	195
ELP Rise Time (min)	61 \pm 32	55 \pm 10	8	140
ELP Decay Time (min)	31 \pm 17	28 \pm 8	4	93
ELP Rise Fraction	0.65 \pm 0.15	0.66 \pm 0.12	0.25	0.91
ELP Decay Fraction	0.35 \pm 0.15	0.34 \pm 0.12	0.09	0.75
Skew	2.36 \pm 1.45	2.10 \pm 0.9	0.15	9.00
ELP-Flare Duration Ratio	5.63 \pm 2.3	4.95 \pm 1.8	1.0	14.5

flare.

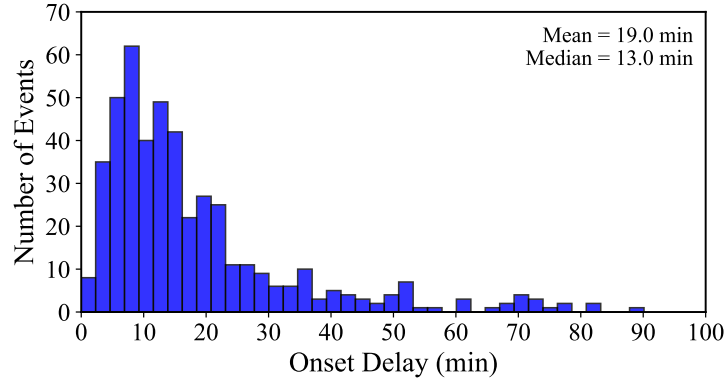


Figure 7: Histogram of the ELP onset delay (Δt_{onset}) distribution in Fe XVI, constructed in 5 minute bins for the 467 validated ELP events. Mean and median values are displayed in the upper-right corner.

3.3.2 Peak-to-Peak Delay

The peak-to-peak delay (Δt_{peak}) represents the time interval between the maximum of the Fe XVI emission during the main flare and the maximum of the corresponding late-phase emission. From Figure 8, it is apparent that the peak delays span a broad range from 8 to 226 minutes. A mean Δt_{peak} of 88 ± 41 minutes and a median of 82 minutes were calculated. The distribution roughly resembles a normal distribution with a moderate asymmetry, with the majority of ELP peaks occurring within two hours of the flare maximum. Only a small number of events ($\sim 3\%$) exhibit peak separations greater than 180 minutes.

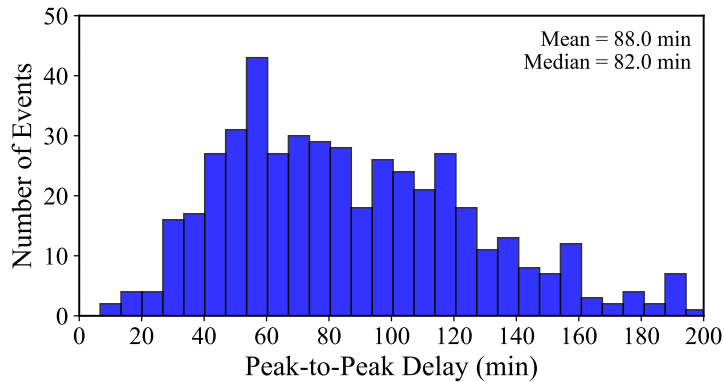


Figure 8: Histogram of the peak-to-peak delay (Δt_{peak}) between the Fe XVI emission maxima of the main flare and the corresponding ELP, constructed in 10 minute bins for the 467 validated events. Mean and median values are displayed in the upper-right corner.

3.3.3 Flare and ELP Durations

Figure 9 presents the distribution of the overall ELP duration (t_{ELP}), defined as the interval between the start and end times of the secondary Fe XVI emission, following the definitions outlined in Section 2.3. Across the sample, ELP durations range from 15 to 195 minutes, with a mean of 93 ± 42 minutes and a median of 89 minutes. The distribution is approximately normal, with most events lasting between one and two hours. The flare durations were similarly defined from the Fe XVI emission, rather than from the standard GOES SXR timings, as the interval between the start and end of the primary Fe XVI brightening. In contrast to the ELP, flare durations are typically much shorter, with a mean of 23 minutes. The ELP duration was found to exceed the flare duration in 98 % of events. The average duration ratio between the ELP and the associated flare (\overline{R}_t) was found by:

$$\overline{R}_t = \frac{1}{N} \sum_{i=1}^N \frac{t_{\text{ELP},i}}{t_{\text{flare},i}} = 5.63 \quad (2)$$

where N is the number of valid ELP events. This indicates that, on average, the Fe XVI emission during the ELP persists for more than five times the duration of the main flare. Figure 10 compares the flare and ELP durations, with points coloured by GOES class, represented on a logarithmic scale for clarity. Individual 1σ uncertainties in duration were estimated via 1000 Monte Carlo resamplings, perturbing each start and end time by Gaussian noise ($\sigma = 1$ min). This value represents the approximate timing precision of the AIA derived lightcurve boundaries. The resulting per-event uncertainties are small compared to the total durations of tens to hundreds of minutes and are therefore

not easily visible in Figure 10. From this distribution, it is evident that the durations of both the flares and their corresponding ELPs are largely independent of flare magnitude and no clear correlation exists between the durations of the two phases.

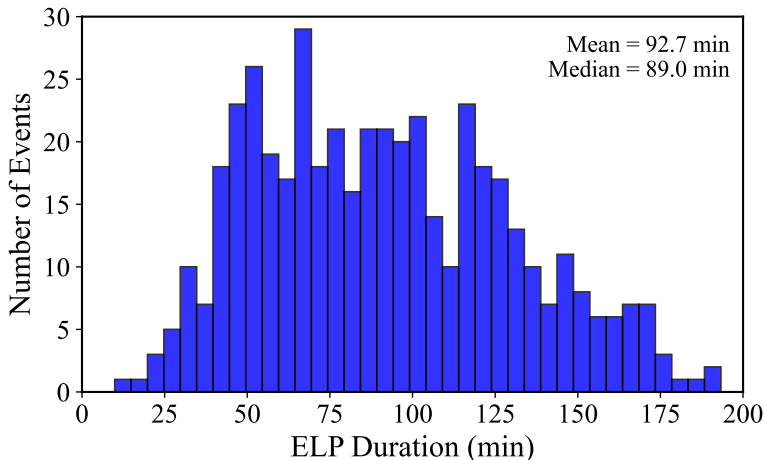


Figure 9: Histogram of the ELP duration (t_{ELP}) in Fe XVI, constructed in 10 minute bins for the 467 validated events. Mean and median values are displayed in the upper-right corner.

3.3.4 Temporal Morphology of the ELP

The temporal evolution of the ELP provides important context for understanding the physical processes driving the emission, and several details can be inferred from the morphology of the Fe XVI timeseries. Figure 11 illustrates the rise (left panel) and decay (right panel) times of the Fe XVI emission during the late-phase. Across the validated sample, the mean rise time was 61 ± 32 minutes, with a median of 55 minutes, whereas the decay time was typically shorter, with a mean of 31 ± 17 minutes and a median of 28 minutes. The corresponding skew parameter, defined as $t_{\text{rise}}/t_{\text{decay}}$, has a mean value of 2.36, indicating that the rise phase is typically much longer than the decay phase. We note that the decay time is measured until the Fe XVI flux returns to 50 % of its peak value, which may slightly underestimate the true duration of the decay phase, particularly in long-lived or slowly cooling events. This approach could introduce a systematic truncation that biases the skew and duration statistics modestly toward shorter values. Nevertheless, this threshold ensures consistency across the sample and mitigates the influence of background drift or post-flare variability.

To quantify the relative contributions of the two stages of the late-phase, the Fe XVI rise and decay times were expressed as fractions of the total late-phase duration. Figure 12 shows the relative fractions of the ELP attributed to the rise

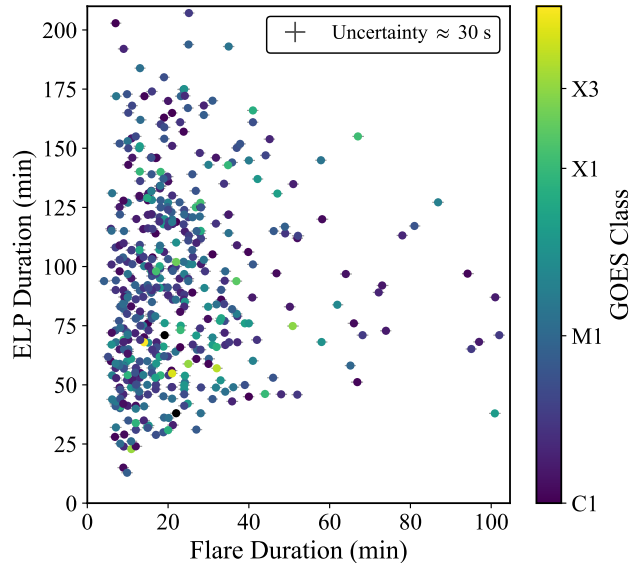


Figure 10: Comparison between flare and ELP durations derived from Fe XVI emission for the 467 validated events. Each point represents an individual flare-ELP pair, coloured by GOES class. Individual measurement uncertainties arise from the 60 s AIA cadence (timing precision of ± 30 s), but these duration errors are small compared to the measurement values and therefore not visible at the scale of the plot.

(left panel) and decay phases (right panel), respectively. Both fractions exhibit broad variability across events, but the late-phase is typically dominated by the rise phase. The blue bars, representing the rise fraction, are centred above 0.5 (ranging from approximately 0.6–0.8), while the red bars, representing the decay fraction, peak below 0.5 (around 0.2–0.4). Averaged over all events, the typical rise and decay fractions were found to be 65 % and 35 %, respectively. This behaviour is consistent with the skew distribution reported above and has implications for the energy-release and transport mechanisms that sustain the ELP.

3.4 Rise and Decay Rates

To further assess the change in ELP flux over time, the rates at which the Fe XVI emission increased and decayed were examined. These rates were calculated as the flux change per unit time during the rise and decay intervals. For each event, the rise rate was defined as $R_{\text{rise}} = (F_{\text{peak}} - F_{\text{start}})/(t_{\text{peak}} - t_{\text{start}})$ and the decay rate as $R_{\text{decay}} = (F_{\text{peak}} - F_{\text{end}})/(t_{\text{end}} - t_{\text{peak}})$.

Figure 13 presents the relationship between the rise and decay rates (R_{rise} , R_{decay}) across the sample. A clear correlation spanning more than three orders of mag-

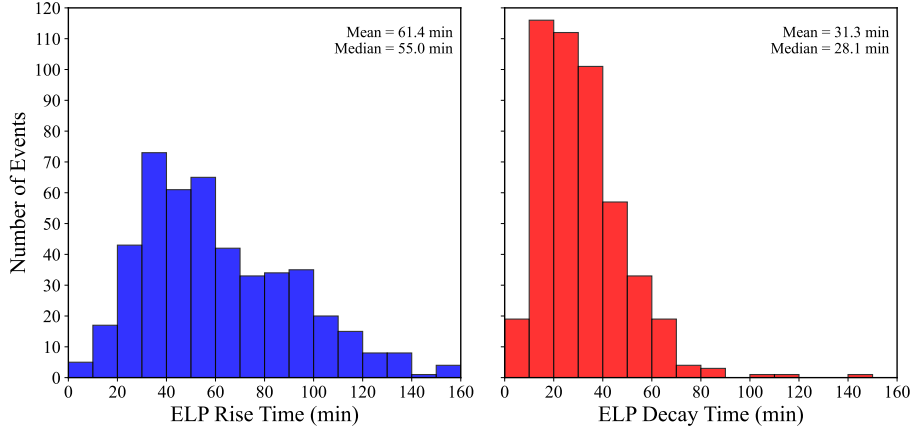


Figure 11: Distributions of the Fe XVI late-phase rise time (left; blue) and decay time (right; red) for the 467 validated events. Each panel shows the corresponding histogram for that interval each in 10 minute bins. Mean and median values are displayed in the upper-right corner of each panel.

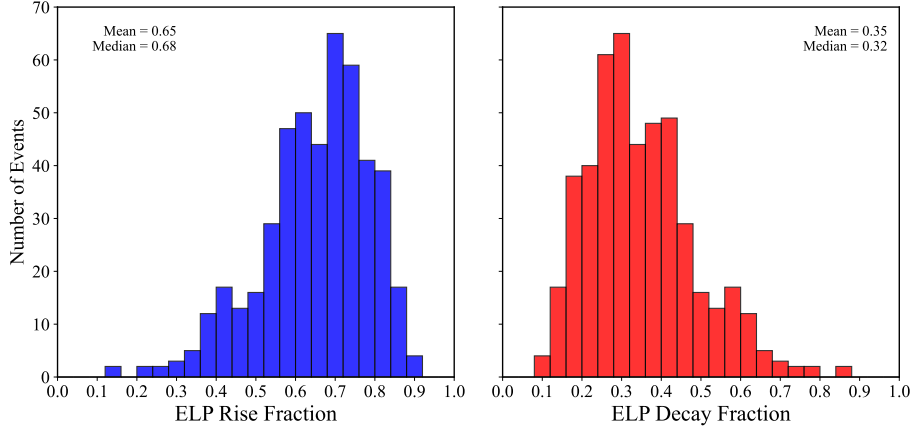


Figure 12: Distributions of the Fe XVI late-phase rise fraction (left; blue) and decay fraction (right; red) for the 467 validated events. The histograms are constructed in bins of 0.5. Each fraction is defined relative to the total ELP duration ($t_{\text{rise}}/t_{\text{ELP}}$ and $t_{\text{decay}}/t_{\text{ELP}}$). Mean and median values are displayed in the upper-right corner of each panel.

nitude was found, with only a small subset of low-rate events showing larger uncertainties due to reduced signal-to-noise. A log-log linear regression yielded a power-law relation of $R_{\text{decay}} = 4.08 R_{\text{rise}}^{0.92}$, with a Pearson correlation coefficient of $r = 0.79 \pm 0.01$ and a Spearman rank coefficient of $\rho = 0.76 \pm 0.01$, both

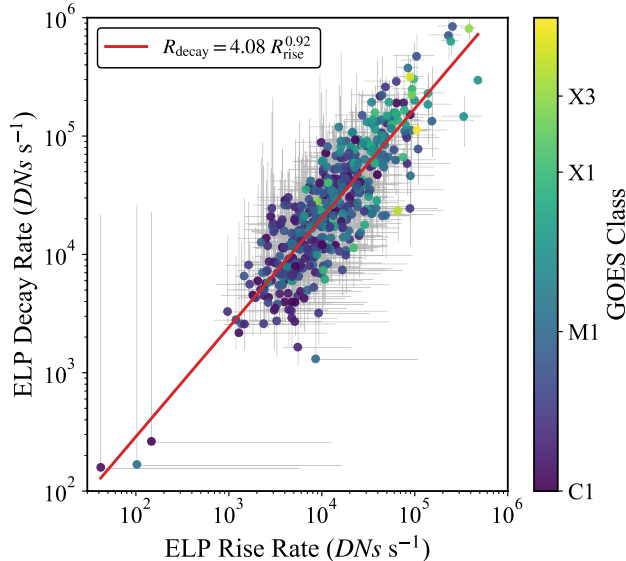


Figure 13: Relationship between the rise and decay rates of the Fe XVI late-phase emission, derived for the 467 validated ELP events. Each point represents an individual flare, colour-coded by GOES class. Error bars denote the 1σ confidence intervals derived from 1000 Monte Carlo resamplings, where measured fluxes were perturbed by Gaussian noise assuming a 5 % fractional photometric uncertainty. The red line indicates the best-fit power-law relation, $R_{\text{decay}} = 4.08 R_{\text{rise}}^{0.92}$, obtained from a log-log linear regression. Pearson and Spearman correlation coefficients were $r = 0.79$ and $\rho = 0.76$, respectively.

indicating a strong positive correlation. The quoted 1σ uncertainties were estimated from 1000 Monte Carlo resamplings of each event, in which the flare and ELP fluxes were perturbed by Gaussian noise adopting a 5 % fractional photometric uncertainty, consistent with the short-term relative radiometric stability of AIA (Boerner et al. 2012, 2014), and the rates were recomputed to propagate per-point measurement errors. A clear dependence on flare magnitude is also evident, with larger flares exhibiting systematically faster rise and decay rates. The near-unity slope demonstrates that these rates increase in a coherent manner, implying that the growth and decay of the Fe XVI late-phase emission may be linked processes.

3.5 Impulsivity and Relative Flux

To examine the rate and relative strength of energy release during the ELP and how this compares to the associated initial flare, an adapted impulsivity parameter was calculated for the main flare and the corresponding ELP for each event in the sample. Figure 14 presents the relationship between flare and

ELP impulsivity for all validated events, with the points once again coloured by GOES class. A clear positive correlation is evident between the impulsivities of the two phases, spanning over three orders of magnitude in flux rate, albeit with a moderate degree of scatter. The best-fit power-law relation, obtained from a log-log linear regression, was $I_{\text{ELP}} = 2.09 I_{\text{flare}}^{0.57}$, with a Pearson correlation coefficient of $r = 0.60 \pm 0.02$ and a Spearman rank coefficient of $\rho = 0.61 \pm 0.02$. Uncertainties were estimated using the same Monte Carlo process as those used for the rise and decay rates, shown as grey error bars in Figure 14. A clear dependence on the flare magnitude is present, where the larger flares feature both a greater impulsivity in the initial flare and subsequent ELP. The sub-linear slope (< 1) of the best-fit power law indicates that ELP impulsivity increases more slowly than flare impulsivity. These findings may have implications for the driving mechanism in the associated energy release of each phase (further discussed in Section 4).

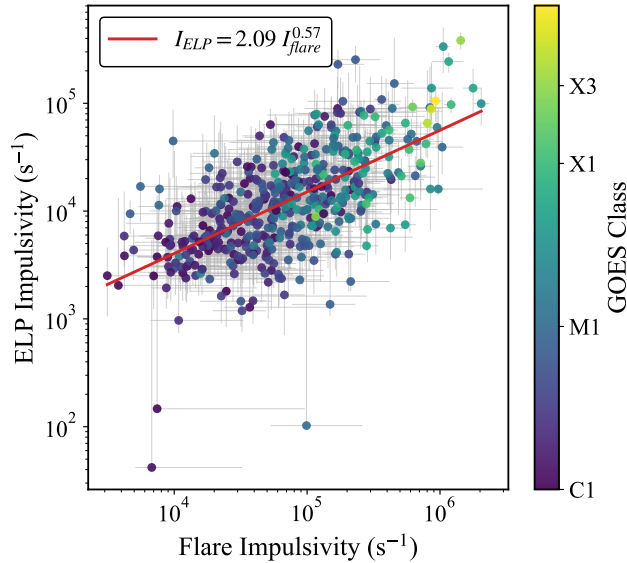


Figure 14: Relationship between the impulsivity of the main flare and the corresponding ELP, calculated from Fe XVI emission for the 467 validated events. Each point represents an individual flare-ELP pair, coloured by GOES class. Error bars denote the 1σ confidence intervals derived from 1000 Monte Carlo resamplings per event, in which the measured fluxes were perturbed by Gaussian noise at the 5 % level. The red line shows the best-fit power-law relation obtained from a log-log linear regression, $I_{\text{ELP}} = 2.09 I_{\text{flare}}^{0.57}$, with Pearson and Spearman correlation coefficients of $r = 0.60$ and $\rho = 0.61$, respectively.

To complement the impulsivity analysis and remove the temporal element from the phase comparison, the relative enhancements of Fe XVI emission were also compared (Figure 15). The mean flare enhancement was 1.17 ± 0.23 , while

the mean ELP enhancement was 1.10 ± 0.08 %, corresponding to average flux increases of 17 % and 10 %, respectively. Uncertainties for each data point were calculated using the same methods as those for the impulsivity. The distribution shows no clear linear relationship between the two quantities, with the majority of events clustered toward lower enhancements and with all events sufficiently scattered. Several events displayed large flare enhancements without equivalent large increases in the ELP, thus no systematic dependence of ELP enhancement on flare class is apparent.

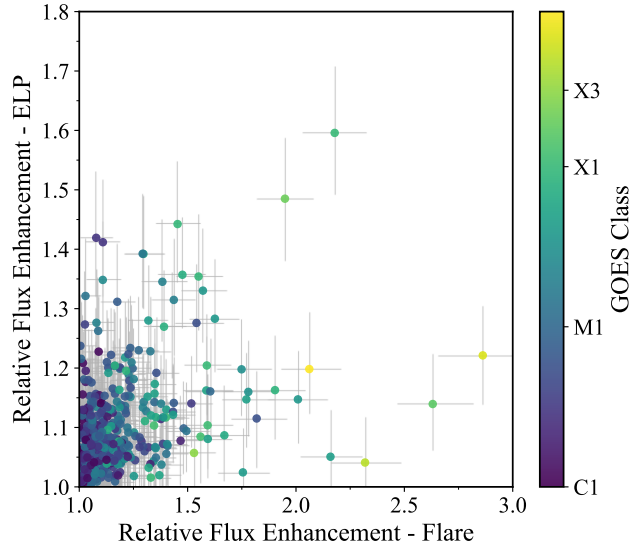


Figure 15: Relationship between the peak relative flux enhancements of the Fe XVI emission during the main flare and the corresponding ELP for the 467 validated events. Each point represents an individual event, coloured by GOES class. The relative enhancement for each phase was calculated as the ratio of the peak flux to the fitted preflare background level. Error bars denote the 1σ uncertainties derived from 1000 Monte Carlo resamplings per event, in which the measured fluxes were perturbed by Gaussian noise assuming a 5 % fractional photometric uncertainty

Comparing the peak enhancements between the two phases, approximately 36 % of the flares in the sample demonstrated Fe XVI enhancements that were greater in the ELP than in the main flare. Thus, only approximately a third of these events may be considered to be extreme ELP events [Chen et al., 2020]. It is important to note that due to the significant workload required to calibrate each individual event over such a large sample, all measurements of flux remain relative for this investigation. Further follow-up investigations may be conducted for a smaller sub-sample of flux-calibrated events to examine ELP energetics and absolute fluxes.

3.6 Correlated Parameters

To explore interdependencies among the derived ELP parameters and test for previously unidentified relationships, pairwise Spearman correlation coefficients were computed between the parameters for all validated ELP events. This analysis considered the variables outlined in Section 3.3 and 3.5 for the flare and ELP emission. The Spearman correlation coefficient was determined to be the most representative parameter in this instance as it better captures nonlinear monotonic relations while being robust to scatter. Figure 16 presents the resulting pairwise Spearman correlation matrices.

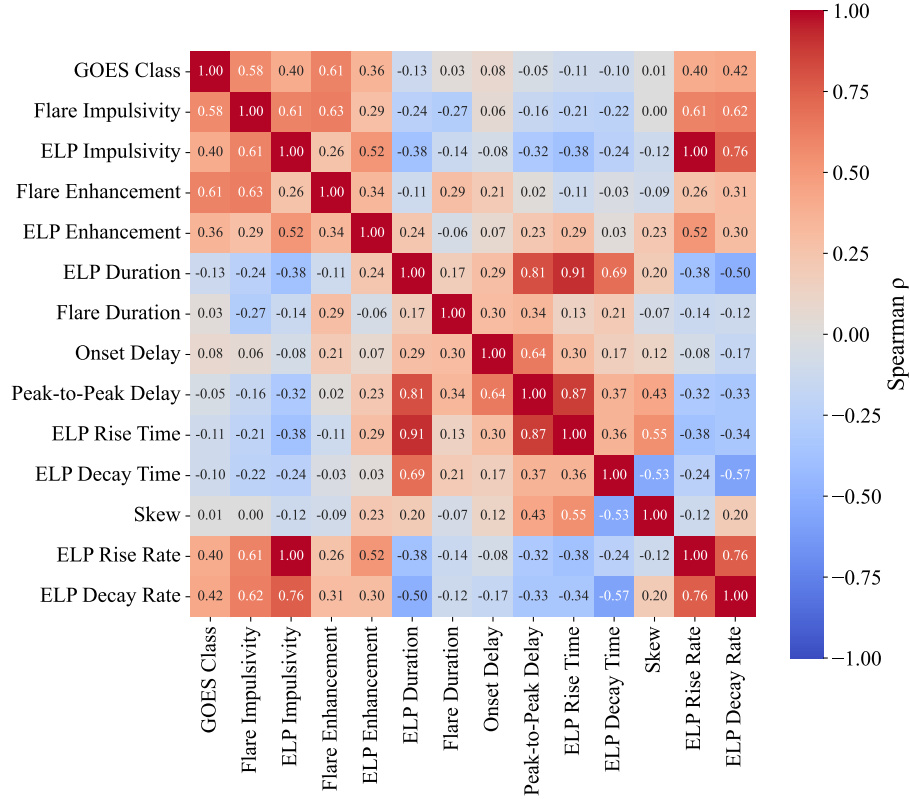


Figure 16: Pairwise Spearman rank correlation matrix for the temporal and morphological parameters of the 467 validated ELP events. Each cell represents the correlation coefficient (ρ) between two quantities derived from the Fe XVI emission. The colour scale indicates the strength and sign of the correlation, with positive values in red and negative values in blue. The annotated values represent the mean ρ obtained from 1000 bootstrap resamplings.

Aside from the correlations already identified, several of the strongest correlations in Figure 16 arise directly from definitional coupling between the parame-

ters, such as the relationship between ELP duration, rise time, and peak-to-peak delay. This is especially true for parameters such as impulsivity, enhancements, and rise and decay rates, as these are effectively separated only by scaling factors. These correlations therefore do not carry physical significance. This analysis does confirm and quantify the finding that several of those parameters have some dependence on the GOES class, and therefore the magnitude of the flare. However, the more informative relationships are those comparing flare parameters with ELP parameters, particularly those related to temporal evolution, which show uniformly low Spearman coefficients ($\rho < 0.30$). In particular, the flare duration is only weakly related to the ELP duration ($\rho = 0.17 \pm 0.04$) and to the ELP rise and decay times ($\rho = 0.13$ and $\rho = 0.21$, respectively). This lack of correlation between these metrics demonstrates that the temporal evolution of the late-phase is largely separate from that of the main flare despite their shared magnetic environment (this is further discussed in Section 4).

3.6.1 Principal Component Analysis

As a further extension to the analysis, a PCA was performed on the quantities examined above to explore the structure of the flare and late-phase parameter space. The results of this analysis are presented in Figure 17. The first three principal components (PCs) were found to capture almost 60 % of the total variance in the dataset, with PC1 representing 26.5 %, PC2 17.8 %, and PC3 15.3 %. The variable loadings in Figure 17a highlight the dominant contributions to each axis. PC1 was primarily aligned with ELP duration (0.50), peak-to-peak delay (0.48), and rise time (0.48), reflecting a shared timescale component in the late-phase evolution. PC2 was most strongly influenced by both ELP impulsivity and ELP rise rate (0.51), which are mathematically similar and reflect the rapidity of late-phase brightening, with additional moderate contributions from flare enhancement (0.30), onset delay (0.30), and ELP decay rate (0.27), suggesting a generalised heating-rate or energy-release axis. PC3 appeared to encode the relative partitioning of energy between the flare and late-phase, with large positive loadings from flare impulsivity (0.47) and enhancement (0.42), and weaker negative contributions from the ELP counterparts. Although ELP impulsivity and rise rate are effectively scaled versions of the same physical quantity, both are retained here to maintain consistency with earlier sections and allow direct comparison with flare-phase and decay-related parameters. The loadings across each PC are summarised in Table 4 along with the variances. Figure 17b shows the PCA-transformed events coloured by GOES class. A slight dependence on flare magnitude is evident, consistent with earlier trends involving rates and impulsivity (Sections 3.4–3.5). While the loadings rarely exceed 0.5 in magnitude, the strongest contributors to each principal component fall within the range typically considered physically meaningful ($|\text{loading}| \geq 0.45$; Jolliffe 2011). The relationships between some high-loading parameters may reflect definitional overlap, and their physical interpretations remain speculative. Further discussion is presented in Section 4.

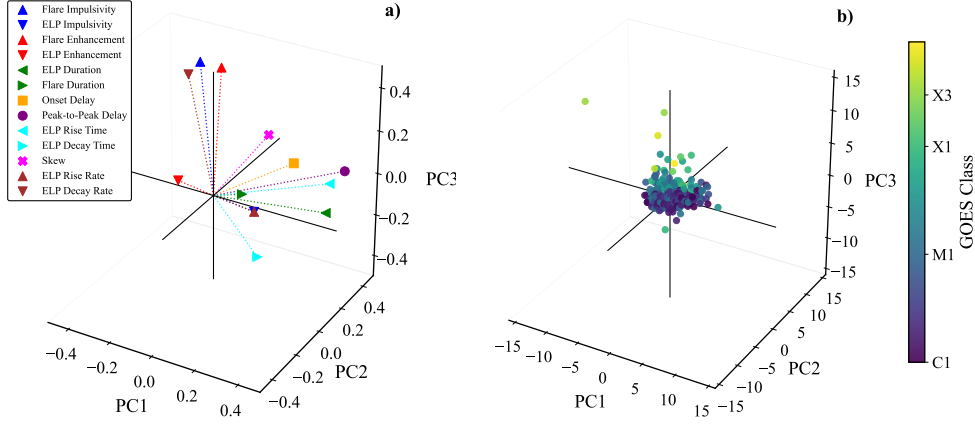


Figure 17: PCA of the flare and EUV late-phase parameters. Panel (a): Loadings of all physical parameters on the first three PCs where each coloured marker represents an individual parameter from those derived from the prior timeseries analysis. The relative strengths of these loadings determine how strongly each parameter contributes to the PC. Panel (b): PCA score distribution, coloured by GOES class, which indicates how strongly each event expresses the characteristics captured by each principal component.

Table 4: PCA results for the 13 flare and EUV late-phase parameters used in this study ($N = 467$). (a) Loadings of each parameter on the first three principal components. (b) Explained variance ratios for PC1–PC3.

(a) PCA Loadings			
Parameter	PC1	PC2	PC3
Onset Delay	0.208	0.305	0.061
Peak-to-Peak Delay	0.484	0.222	0.142
Flare Duration	0.086	0.085	-0.012
ELP Duration	0.495	0.039	0.043
ELP Rise Time	0.483	0.092	0.148
ELP Decay Time	0.251	-0.080	-0.175
Skew	0.176	0.143	0.262
ELP Rise Rate	-0.091	0.512	-0.365
ELP Decay Rate	-0.273	0.265	0.369
Flare Impulsivity	-0.183	0.209	0.474
ELP Impulsivity	-0.091	0.512	-0.365
Flare Enhancement	-0.133	0.297	0.422
ELP Enhancement	0.009	-0.294	0.219

(b) Explained Variance Ratio		
PC1	PC2	PC3
0.265	0.178	0.153

4 Discussion

The results presented in this study provide new insight into the occurrence and temporal behaviour of the EUV late-phase in solar flares, based exclusively on Fe XVI (335 Å) emission observed by SDO/AIA. Across the 15 year dataset, validated ELPs were found in approximately 8 % of isolated flares, which is a lower than previously reported in studies using disk-integrated SDO/EVE observations [Woods et al., 2011, Woods, 2014, Chen et al., 2020, Ornig et al., 2025]. This reduction is not attributable to a single factor, but likely reflects a combination of differences in methodology, instrumentation, and sample composition. For example, the present work incorporates a more temporally expansive and statistically representative flare sample that includes both solar maximum and minimum conditions, and extends the flare selection threshold down to GOES C1.0, compared to C3.0 or higher in prior studies. Both of these choices can reduce the relative ELP detection rate by including a larger proportion of weaker or morphologically simple events, which are less likely to exhibit a pronounced late-phase.

The exclusive use of spatially resolved AIA observations, rather than full-disk EVE irradiance data, also contributes to statistical differences. A direct comparison between instruments revealed a 20 % classification disagreement, highlighting the role of instrumental design and observational context. Several factors can lead to mismatches, including differing sensitivity to Fe XVI, distinct bandpasses, and systematic artefacts [Greatest et al., 2024]. In the majority of discrepant cases, AIA detects a clear ELP while EVE does not. This often occurs during periods of high solar activity, when emission from multiple active regions contributes to the full-disk EVE signal. In such scenarios, contamination from unrelated regions can obscure or dilute the flare-associated Fe XVI enhancement, particularly for weaker or spatially compact events. The spatial resolution of AIA circumvents this by isolating the flare source region, allowing robust identification even when the integrated signal remains ambiguous. Conversely, a smaller fraction of cases exhibit the opposite behaviour, whereby an ELP is identifiable in EVE but not in AIA. These typically involve events where the late-phase emission extends beyond the 500×500 arcsec AIA cutout or is spatially fragmented across disconnected regions. In such cases, the fixed cutout misses the full extent of the emission, while EVE retains sensitivity to the global EUV response. Additional complications may arise from coronal dimming, post-eruptive absorption, or magnetic reconfiguration, all of which can redistribute or obscure ELP emission outside the AIA field of view [López et al., 2017, Dissauer et al., 2018, Toriumi and Wang, 2019]. Ultimately, this study was necessarily focussed on spatially constrained observations, which while not immune to observational shortcomings, gave a robust, isolated detection of the ELP from flare active regions. The lower overall occurrence rate reported here should therefore be understood as the result of a more inclusive sample, broader temporal coverage, and spatially resolved methodology, rather than a limitation or contradiction of earlier work.

In this study, we identify that only around one third of the ELP events in

our sample qualify as extreme late-phases, where the Fe XVI flux exceeds that of the main flare. This is significantly fewer than reported by Chen et al. [2020] and Ornić et al. [2025], and likely arises from our inclusion of weaker flares, the application of a more permissive ELP threshold, and the use of a much larger sample size. No significant dependence of ELP occurrence on the solar cycle was identified, with the detection rate remaining broadly consistent throughout the 15 year period, which is the longest temporal baseline examined to date. This consistency suggests that while the absolute number of ELPs scales with the overall flare rate, their relative frequency remains constant across changing activity levels. Beyond occurrence statistics, the temporal morphology of the Fe XVI emission provides further insight into the nature of the late-phase. A strong positive correlation was identified between the rise and decay rate of the ELP ($r = 0.79$, $\rho = 0.76$). Indicating that flares with a faster rate of increase also tended to have a faster decay rate. A clear positive correlation was also found between the impulsivities of the flare and ELP phases ($r = 0.60$, $\rho = 0.61$), indicating that, on an event-by-event basis, more impulsive flares tend to be followed by proportionally more impulsive late-phases. These relationships may hint at a coupling between the energy release of the two phases, rather than a single common ELP mechanism operating identically in all cases.

An important result from this study is the strong correlation between the Fe XVI rise and decay rates during the late-phase. The rates span over three orders of magnitude yet follow a coherent power-law relation, with greater rise rates accompanied by proportionally greater decay rates. This behaviour suggests that the processes governing the increase and subsequent decline of the warm coronal emission evolve coherently. If the late-phase is powered by continued or secondary reconnection, then both the brightening and cooling rates may scale with the magnetic energy release and the geometry of the overlying loop system [Woods et al., 2011, Dai et al., 2013, Liu et al., 2015]. Conversely, in cooling-dominated cases, long and dense coronal loops naturally produce slower rises and slower decays, as both conductive and radiative cooling timescales increase with loop length and plasma density [Cargill et al., 1995a, Woods, 2014]. The near-unity slope of the relation therefore accommodates both scenarios and implies that, irrespective of whether renewed heating or extended cooling dominates, the temporal evolution of the late-phase is governed by a common underlying physical structure in the active region. The small population of low-rate events with large uncertainties likely reflects cases where the late-phase emission is weak relative to background levels or where the geometry produces very gradual evolution [Woods et al., 2011].

Another key result from this study is the scaling relationship between the impulsivity of the main flare and that of the ELP. One possible conclusion from this finding is that both phases share a common dependence on the magnetic properties of their associated active region. Tamburri et al. [2024] reported that larger EUV impulsivities correspond to stronger magnetic reconnection rates, implying that the impulsive evolution is magnetically mediated. Although we do not directly examine the magnetic topology of the ELP regions, other studies have similarly found links between magnetic configuration and late-phase

emission [Woods et al., 2011, Ornig et al., 2025]. Despite this, it must be acknowledged that two potential mechanisms can produce late-phase emission: continued or secondary reconnection and extended cooling of large, overlying flare loops. Variability in impulsivity among events may therefore arise from differences in the dominant process. In cooling-dominated cases, the rise rate of Fe XVI emission is governed primarily by conductive and radiative cooling timescales, which depend on loop length, temperature, and density [Cargill et al., 1995b]. This naturally broadens the impulsivity distribution and may explain the scatter around the observed scaling relation. Some of the more weakly correlated events could correspond to confined flares that do not significantly alter the overlying magnetic structure [Aschwanden et al., 2009, Woods et al., 2011], where extended cooling dominates over renewed energy release. Ultimately, it is not possible to determine the dominant driver of each ELP solely from the emission timeseries. Nevertheless, the proportional relationship between flare and ELP impulsivities carries important implications for the terrestrial response, whereby rapid energy injection into the upper atmosphere during the main flare may often be followed by a proportionally rapid secondary injection during the late-phase, on timescales characterised by the onset and peak-to-peak delays. We also find that greater magnitude flares typically exhibit a more impulsive ELP but not necessarily a higher ELP occurrence rate, indicating that additional factors, such as the active region topology, remain decisive in determining whether a late-phase forms at all.

The PCA results further support the interpretation that ELP evolution is governed by several physically distinct processes, a summary of the PCA results is presented for succinctness in Table 5. PC1 captures the fundamental timescale behaviour of the ELP, with strong positive loadings on duration, rise time, and peak delay, indicative of a dependence of ELP emission on components that may be governed by loop sizes and reconnection timescales [Woods et al., 2011, Chen et al., 2020]. PC2, meanwhile, is primarily driven by ELP impulsivity and rise rate, which are functionally similar quantities, and represents an axis of energy release intensity. The inclusion of flare impulsivity on this component, partnered with the premise that impulsivity may depend on reconnection rate in the active region [Tamburri et al., 2024], suggests that more magnetically dynamic active regions may tend to produce stronger, more impulsive heating episodes in both the flare and late-phase systems. Additionally, the onset delay as a secondary contributor to PC2 supports the interpretation of this component as representing the timing and intensity of energy delivery into the ELP system, where shorter delays may reflect more efficient or immediate energisation of the overlying loops. PC3 is more complex, with large positive loadings from flare impulsivity and rise rate and moderate negative loadings from ELP impulsivity and rise rate. This structure may reflect a partitioning of the available magnetic energy between the flare and the ELP. In this scenario, flare events may exhibit stronger impulsivity and peak enhancement, with comparatively weaker or more gradual ELP evolution, while ELP-dominated cases reflect the opposite [Chen et al., 2020]. The moderate negative loading of ELP enhancement on PC2 also raises the possibility of a trade-off between impulsivity and total ra-

diative output in the late-phase, perhaps indicative of a finite magnetic energy budget within the active region if we consider the enhancement measure to be a feasible proxy for energy release. For example, consider the reconnection driven scenario for ELP generation, the energy budget available to the initial flare is governed by the available magnetic free energy to be released [Emslie et al., 2012, Aschwanden et al., 2017]. If this flare releases a substantial portion of that available energy, a comparatively weaker ELP release would be explained by the lower available energy in the overlying loop system available for release, and it is known that the geometry and reconnection process impose an upper limit on what fraction of the free energy can be converted in an event [Aulanier et al., 2013, Dai et al., 2013]. Yet, the general linear, GOES class dependent, relationship between flare and ELP impulsivity discussed above is still justified, as the impulsivity measure also considers the timescale of the release as well as the magnitude. This could also explain why smaller flares sometimes exhibit large ELP peaks, exemplified by findings from Bekker et al. [2024]. It is important to note that these interpretations remain speculative and should not be overinterpreted. Future studies incorporating direct magnetic diagnostics and energetic modelling will be essential to test these hypotheses and more fully constrain the drivers of PCA variability.

Table 5: Summary of the three principal components derived from PCA of flare and ELP parameters. Each component is labelled with its physical interpretation, the percentage of variance it explains, and the three primary contributing parameters with their corresponding loading values.

PC	Physical Interpretation	Explained Variance (%)	Primary Parameters
PC1	ELP Temporal Evolution	26.5	ELP Duration (0.50)
			ELP Rise Time (0.48)
			Peak-to-Peak Delay (0.48)
PC2	Energy Release	17.8	ELP Impulsivity & Rise Rate (0.51)
			Flare Enhancement (0.30)
			Onset Delay (0.30)
PC3	Flare-ELP Energy Partition	15.3	Flare Impulsivity (0.47)
			Flare Enhancement (0.42)
			ELP Decay Rate (0.37)

The onset of the ELP typically followed the end of the main flare by approximately 19 minutes, while the delay between the flare and ELP peaks was around 88 minutes, in good agreement with previous studies [Woods et al., 2011, Woods, 2014, Orniq et al., 2025]. Slight discrepancies in timing may arise from the use of 60 s cadence SDO/AIA images compared to 10 s SDO/EVE data and the larger number of events analysed, but these differences are minor. Only 36 % of the sample exhibited onset delays greater than 20 minutes, beyond which the distribution became significantly more dispersed. This suggests that longer delays may be governed by the cooling timescales of the overlying flare loops, which are more variable than the reconnection timescales likely responsible for

the faster onsets

The average ELP duration was approximately 93 minutes, consistent with previous observations using SDO/EVE. This duration was found to be unrelated to either the flare duration or its magnitude. As reported by Ornić et al. [2025], the ELP duration is well correlated with the peak-to-peak delay, here with a comparable Spearman coefficient ($\rho = 0.81$). We also find that both the ELP duration and the peak-to-peak delay are strongly correlated with the ELP rise time ($\rho = 0.91$ and $\rho = 0.87$, respectively). This suggests that the rise phase dominates the overall ELP evolution, consistent with the results in Section 3.3.4, where the rise phase was typically found to last twice as long as the decay phase and to constitute roughly two thirds of the total ELP duration. Interestingly, the temporal parameters defining the ELP show minimal correlation with those of the main flare (typically $|\rho| < 0.3$), indicating that while the two phases are temporally distinct, their impulsivity relationship implies that they remain linked by their driving mechanisms.

Together, these relationships provide key context for understanding the physical mechanisms underlying ELP emission and serve as a benchmark for future classification or predictive models. Moreover, the occurrence statistics, solar cycle invariance, and measured temporal parameters presented here are directly applicable to assessing the terrestrial impact of ELP emission, which is which is invaluable to our understanding of the Sun-Earth connection. We note, however, that the present analysis relies on relative Fe XVI fluxes rather than absolute irradiances and does not directly incorporate magnetic field measurements. Future work combining these temporal diagnostics with vector magnetograms and irradiance calibration will be critical for distinguishing reconnection-dominated and cooling-dominated late-phases and quantifying their respective energy contributions.

While this study focuses on Fe XVI emission, the Fe XV (284 Å) line is known to exhibit a similarly distinct late-phase component and has been shown to have a stronger influence on ionospheric ionisation [Bekker et al., 2024]. Given their closely overlapping formation temperatures (2.5–4.0 MK) and correlated behaviour during flares, Fe XVI serves as a physically justified proxy for Fe XV in characterising the late-phase evolution. Accordingly, the diagnostics presented here are expected to be directly applicable to studies of ionospheric response to ELP emission.

5 Conclusions

This study presents the statistical analysis of 467 ELP events identified from a sample of 5335 isolated flares observed by SDO/AIA between 2010 and 2025, constituting the largest and most temporally extended analysis of EUV late-phase behaviour to date. This work focuses on the occurrence rate, class dependence, and solar cycle variability of the ELP, as well as on several metrics that have implications for understanding the physical origin of ELP emission and its corresponding impact on the terrestrial atmosphere.

The overall ELP occurrence rate was approximately 8 %, lower than in previous analyses based on disk-integrated SDO/EVE data. This difference may be attributed to both the larger, more representative flare sample, and the exclusive use of SDO/AIA measurements. No significant dependence of ELP occurrence on the solar cycle was identified, and only a weak dependence on flare magnitude was observed, with a modest preference for the low-mid M-class range (M3.0–M5.9). The rise and decay rates of the ELP were found to be tightly correlated over three orders of magnitude, suggesting that the processes governing the growth and decline of warm coronal emission evolve coherently. Additionally, a clear scaling relation was found between the impulsivity of the main flare and that of the ELP, indicating a potential link between the two phases through their shared magnetic environment. The typical onset and peak-to-peak delays of 19 and 88 minutes, respectively, together with the average ELP duration of 93 minutes, are consistent with earlier studies but derived here from a more extensive dataset. A pairwise correlation analysis of the temporal parameters of both phases revealed minimal dependence of the ELP evolution on the temporal characteristics of the flare, reinforcing the notion that, while energetically linked, the ELP is temporally distinct from the main flare. Principal Component Analysis further revealed that three dominant axes may explain the majority of the variability in flare-ELP morphology. The first component represented a global timescale axis, dominated by ELP duration and rise timing. The second captured the overall intensity and impulsivity of energy release. The third reflected a potential partitioning of energy between the flare and ELP phases. Together, these results reinforce that ELP behaviour is not solely dependent on flare magnitude, but instead reflects a combination of magnetic topology and energy transport processes. While speculative, these interpretations are physically motivated and may serve as a useful framework for future investigations.

The results presented here provide a benchmark characterisation of the behaviour of the EUV late-phase, further highlighting that while the ELP is relatively rare, its occurrence and dynamics are likely governed by active-region magnetic structure and plasma-cooling processes, although these were not explicitly explored in this analysis. The statistical relationships reported here and the derived parameters are directly relevant to models of flare-associated emission such as the *Flare Irradiance Spectral Model* (FISM; Chamberlin et al. 2007, 2020, Chamberlin et al. 2025) and provide an empirical foundation for assessing the ionospheric response to delayed EUV radiation. The analysis is necessarily limited by the use of relative, rather than absolute, Fe XVI fluxes and by the absence of direct magnetic field measurements. Future work combining these diagnostics with magnetic extrapolations and irradiance-calibrated datasets will be essential for identifying the physical origins of late-phases and quantifying their respective energy budgets.

Finally, this work builds upon and extends previous statistical studies of the EUV late-phase by taking full advantage of the long-term, multi-wavelength coverage provided by SDO/AIA. The continuity of AIA observations has enabled the first systematic investigation of ELP behaviour over nearly two solar cycles

using exclusively spatially-resolved diagnostics. These data continue to provide an essential foundation for advancing our understanding of solar flare evolution, the dynamics of the solar atmosphere, and the influence of solar activity on the terrestrial environment.

6 Acknowledgements

H.J.G, R.J.C, and R.O.M would like to thank the UK’s Science & Technology Facilities Council (ST/X000923/1) for supporting this research. A.N.O, S.B, and R.O.M would like to thank the European Office of Aerospace Research and Development (FA8655-22-1-7044-P00001) for supporting this research. This work was also supported by the International Space Science Institute (ISSI) in Bern, through ISSI International Team project #24-618.

7 Data Availability

No new data was created as part of this study. SDO/AIA data may be accessed through the *Joint Science Operations Centre* (JSOC; <http://jsoc.stanford.edu/>). SDO/EVE data may be accessed via the EVE data site or directly here: https://lasp.colorado.edu/eve/data_access/index.html. SXR data are publicly accessible from GOES-16 via <https://www.ncei.noaa.gov/products/goes-r-extreme-ultraviolet-xray-irradiance> and from GOES-14 and -15 via <https://www.ncei.noaa.gov/products/goes-1-15/space-weather-instruments>. All observation data in this study were analysed using sunpy (<https://sunpy.org/>; The SunPy Community et al. 2020) and aiapy packages (<https://zenodo.org/records/17114673>; Barnes et al. 2020).

References

- M. J. Aschwanden. Particle acceleration and kinematics in solar flares. *Space Science Reviews*, 101:1–227, 2002. doi: 10.1023/A:1019712124366.
- M. J. Aschwanden, J. P. Wuelser, N. V. Nitta, and J. R. Lemen. Solar Flare and CME Observations with STEREO/EUVI. *Sol. Phys.*, 256(1-2):3–40, May 2009. doi: 10.1007/s11207-009-9347-4.
- Markus J. Aschwanden, Amir Caspi, Christina M. S. Cohen, Gordon Holman, Ju Jing, Matthieu Kretzschmar, Eduard P. Kontar, James M. McTiernan, Richard A. Mewaldt, Aidan O’Flannagain, Ian G. Richardson, Daniel Ryan, Harry P. Warren, and Yan Xu. Global Energetics of Solar Flares. V. Energy Closure in Flares and Coronal Mass Ejections. *Astrophys. J.*, 836(1):17, February 2017. doi: 10.3847/1538-4357/836/1/17.
- G. Aulanier, P. Démoulin, C. J. Schrijver, M. Janvier, E. Pariat, and B. Schmieder. The standard flare model in three dimensions. II. Upper

- limit on solar flare energy. *Astron. Astrophys.*, 549:A66, January 2013. doi: 10.1051/0004-6361/201220406.
- Will T. Barnes, Mark C. M. Cheung, Monica G. Bobra, Paul F. Boerner, Georgios Chintzoglou, Drew Leonard, Stuart J. Mumford, Nicholas Padmanabhan, Albert Y. Shih, Nina Shirman, David Stansby, and Paul J. Wright. aiapy: A python package for analyzing solar evv image data from aia. *Journal of Open Source Software*, 5(55):2801, 2020. doi: 10.21105/joss.02801. URL <https://doi.org/10.21105/joss.02801>.
- S. Z. Bekker and J. A. Korsunskaya. Influence of the Neutral Atmosphere Model on the Correctness of Simulation the Electron and Ion Concentrations in the Lower Ionosphere. *Journal of Geophysical Research (Space Physics)*, 128(12):e2023JA032007, December 2023. doi: 10.1029/2023JA032007.
- S. Z. Bekker, R. O. Milligan, and I. A. Ryakhovsky. Response of ionospheric total electron content to the impulsive and late phases of x-class solar flares with various center-to-limb locations. *Journal of Geophysical Research: Space Physics*, 130(10):e2025JA034281, 2025. doi: <https://doi.org/10.1029/2025JA034281>. URL <https://agupubs.onlinelibrary.wiley.com/doi/abs/10.1029/2025JA034281>. e2025JA034281 2025JA034281.
- Susanna Bekker, Ryan O. Milligan, and Ilya A. Ryakhovsky. The Influence of Different Phases of a Solar Flare on Changes in the Total Electron Content in the Earth’s Ionosphere. *Astrophys. J.*, 971(2):188, August 2024. doi: 10.3847/1538-4357/ad631d.
- P. F. Boerner, P. Testa, H. Warren, M. A. Weber, and C. J. Schrijver. Photometric and Thermal Cross-calibration of Solar EUV Instruments. *Sol. Phys.*, 289(6):2377–2397, June 2014. doi: 10.1007/s11207-013-0452-z.
- Paul Boerner, Christopher Edwards, James Lemen, Adam Rausch, Carolus Schrijver, Richard Shine, Lawrence Shing, Robert Stern, Theodore Tarbell, Alan Title, C Jacob Wolfson, Regina Souffi, Eberhard Spiller, Eric Gullikson, David McKenzie, David Windt, Leon Golub, William Podgorski, Paola Testa, and Mark Weber. Initial calibration of the atmospheric imaging assembly (AIA) on the solar dynamics observatory (SDO). *Solar Physics*, 275(1):41–66, January 2012.
- Paul Boerner, Christopher Edwards, James Lemen, Adam Rausch, Carolus Schrijver, Richard Shine, Lawrence Shing, Robert Stern, Theodore Tarbell, Alan Title, C. Jacob Wolfson, Regina Souffi, Eberhard Spiller, Eric Gullikson, David McKenzie, David Windt, Leon Golub, William Podgorski, Paola Testa, and Mark Weber. Initial Calibration of the Atmospheric Imaging Assembly (AIA) on the Solar Dynamics Observatory (SDO). *Sol. Phys.*, 275(1-2):41–66, January 2012. doi: 10.1007/s11207-011-9804-8.
- Peter J. Cargill, John T. Mariska, and Spiro K. Antiochos. Cooling of Solar Flare Plasmas. I. Theoretical Considerations. *Astrophys. J.*, 439:1034, February 1995a. doi: 10.1086/175240.

- Peter J. Cargill, John T. Mariska, and Spiro K. Antiochos. Cooling of Solar Flare Plasmas. I. Theoretical Considerations. *Astrophys. J.*, 439:1034, February 1995b. doi: 10.1086/175240.
- H. Carmichael. A Process for Flares. In *NASA Special Publication*, volume 50, page 451. 1964.
- P. C. Chamberlin, F. G. Eparvier, V. Knoer, H. Leise, A. Pankratz, M. Snow, B. Templeman, E. M. B. Thiemann, D. L. Woodraska, and T. N. Woods. The flare irradiance spectral model-version 2 (fism2). *Space Weather*, 18(12):e2020SW002588, 2020. doi: <https://doi.org/10.1029/2020SW002588>. URL <https://agupubs.onlinelibrary.wiley.com/doi/abs/10.1029/2020SW002588>. e2020SW002588 10.1029/2020SW002588.
- Phillip Chamberlin, S. Bahauddin, B. Schwab, and E. Thiemann. The Next Generation of Flare Irradiance Spectral Models: FISM-3 and FISM-AI. In *SDO 2025 Science Workshop: A Gathering of the Helio-hive!*, page 180, February 2025.
- Phillip C. Chamberlin, Thomas N. Woods, and Francis G. Eparvier. Flare irradiance spectral model (fism): Daily component algorithms and results. *Space Weather*, 5(7), 2007. doi: <https://doi.org/10.1029/2007SW000316>. URL <https://agupubs.onlinelibrary.wiley.com/doi/abs/10.1029/2007SW000316>.
- Yao Chen, Yuming Wang, Liang Zhao, Xueshang Feng, Chenglong Shen, and Rui Liu. Extreme ultraviolet late phase of solar flares. *The Astrophysical Journal Supplement Series*, 247:53, 2020. doi: 10.3847/1538-4365/ab6a22. URL <https://ui.adsabs.harvard.edu/abs/2020ApJS..247...53C>.
- Y. Dai, M. D. Ding, and Y. Guo. Production of the Extreme-ultraviolet Late Phase of an X Class Flare in a Three-stage Magnetic Reconnection Process. *Astrophys. J. Lett.*, 773(2):L21, August 2013. doi: 10.1088/2041-8205/773/2/L21.
- Yu Dai and Mingde Ding. Probing the Production of Extreme-ultraviolet Late-phase Solar Flares Using the Model Enthalpy-based Thermal Evolution of Loops. *Astrophys. J.*, 857(2):99, April 2018. doi: 10.3847/1538-4357/aab898.
- G. del Zanna, A. Berlicki, B. Schmieder, and H. E. Mason. A Multi-Wavelength Study of the Compact M1 Flare on October 22, 2002. *Sol. Phys.*, 234(1): 95–113, March 2006. doi: 10.1007/s11207-006-0016-6.
- L. Didkovsky, D. Judge, S. Wieman, T. Woods, and A. Jones. Euv spectrophotometer (esp) in extreme ultraviolet variability experiment (eve): Algorithms and calibrations. *Solar Physics*, 275(1):179–205, 2012. ISSN 1573-093X. doi: 10.1007/s11207-009-9485-8. URL <https://doi.org/10.1007/s11207-009-9485-8>.

- K. Dissauer, A. M. Veronig, M. Temmer, T. Podladchikova, and K. Vanninathan. Statistics of Coronal Dimmings Associated with Coronal Mass Ejections. I. Characteristic Dimming Properties and Flare Association. *Astrophys. J.*, 863(2):169, August 2018. doi: 10.3847/1538-4357/aad3c6.
- A. G. Emslie, B. R. Dennis, A. Y. Shih, P. C. Chamberlin, R. A. Mewaldt, C. S. Moore, G. H. Share, A. Vourlidas, and B. T. Welsch. Global Energetics of Thirty-eight Large Solar Eruptive Events. *Astrophys. J.*, 759(1):71, November 2012. doi: 10.1088/0004-637X/759/1/71.
- G. H. Fisher, R. C. Canfield, and A. N. McClymont. Flare Loop Radiative Hydrodynamics. VI. Chromospheric Evaporation due to Heating by Nonthermal Electrons. *Astrophys. J.*, 289:425–433, February 1985. doi: 10.1086/162902.
- Harry J. Greatorex, Ryan O. Milligan, and Ingolf E. Dammasch. On the Instrumental Discrepancies in Lyman-Alpha Observations of Solar Flares. *Sol. Phys.*, 299(11):162, November 2024. doi: 10.1007/s11207-024-02407-7.
- Frederick A. Hanser and Francis Bach Sellers. Design and calibration of the GOES-8 solar x-ray sensor: the XRS. In Edward R. Washwell, editor, *GOES-8 and Beyond*, volume 2812, pages 344 – 352. International Society for Optics and Photonics, SPIE, 1996. doi: 10.1117/12.254082. URL <https://doi.org/10.1117/12.254082>.
- Laura A. Hayes, Oscar S. D. O’Hara, Sophie A. Murray, and Peter T. Gallagher. Solar flare effects on the earth’s lower ionosphere. *Solar Physics*, 296(11), Nov 2021. ISSN 1573-093X. doi: 10.1007/s11207-021-01898-y. URL <http://dx.doi.org/10.1007/s11207-021-01898-y>.
- T. Hirayama. Theoretical Model of Flares and Prominences. I: Evaporating Flare Model. *Sol. Phys.*, 34(2):323–338, February 1974. doi: 10.1007/BF00153671.
- R. A. Hock, T. N. Woods, J. A. Klimchuk, F. G. Eparvier, and A. R. Jones. The Origin of the EUV Late Phase: A Case Study of the C8.8 Flare on 2010 May 5. *arXiv e-prints*, art. arXiv:1202.4819, February 2012. doi: 10.48550/arXiv.1202.4819.
- G. D. Holman, M. J. Aschwanden, H. Aurass, M. Battaglia, P. C. Grigis, E. P. Kontar, W. Liu, P. Saint-Hilaire, and V. V. Zharkova. Implications of X-ray Observations for Electron Acceleration and Propagation in Solar Flares. *Space Sci. Rev.*, 159(1-4):107–166, September 2011. doi: 10.1007/s11214-010-9680-9.
- H. S. Hudson. Solar flares, microflares, nanoflares, and coronal heating. *Solar Physics*, 133:357–369, 1991. doi: 10.1007/BF00149894.
- H. S. Hudson, I. G. Hannah, and T. Kawate. The preflare phase of solar flares and its magnetic interpretation. *Solar Physics*, 296:87, 2021. doi: 10.1007/s11207-021-01824-7.

- N. Hurlburt, M. Cheung, C. Schrijver, L. Chang, S. Freeland, S. Green, C. Heck, A. Jaffey, A. Kobashi, D. Schiff, J. Serafin, R. Seguin, G. Slater, A. Somani, and R. Timmons. Heliophysics Event Knowledgebase for the Solar Dynamics Observatory (SDO) and Beyond. *Sol. Phys.*, 275(1-2):67–78, January 2012. doi: 10.1007/s11207-010-9624-2.
- Ian Jolliffe. Principal component analysis. In *International encyclopedia of statistical science*, pages 1094–1096. Springer, 2011.
- James A. Klimchuk. On Solving the Coronal Heating Problem. *Sol. Phys.*, 234(1):41–77, March 2006. doi: 10.1007/s11207-006-0055-z.
- R. A. Kopp and G. W. Pneuman. Magnetic reconnection in the corona and the loop prominence phenomenon. *Sol. Phys.*, 50(1):85–98, October 1976. doi: 10.1007/BF00206193.
- James Lemen, Alan Title, David Akin, Paul Boerner, Catherine Chou, Jerry Drake, Dexter Duncan, Christopher Edwards, Frank Friedlaender, Gary Heyman, Neal Hurlburt, Noah Katz, Gary Kushner, Michael Levay, Russell Lindgren, Dnyanesh Mathur, Edward McFeaters, Sarah Mitchell, Roger Rehse, and Nick Waltham. The atmospheric imaging assembly (aia) on the solar dynamics observatory (sdo). *Solar Physics*, 275:17–40, 01 2011. doi: 10.1007/s11207-011-9776-8.
- L. A. Leonovich, E. L. Afrainovich, E. B. Romanova, and A. V. Tschilin. Estimating the contribution from different ionospheric regions to the TEC response to the solar flares using data from the international GPS network. *Annales Geophysicae*, 20(12):1935–1941, December 2002. doi: 10.5194/angeo-20-1935-2002.
- Jing Liu, Liying Qian, Wenbin Wang, Kevin Pham, Xiangliang Kong, Yao Chen, Wenlong Liu, Libo Liu, and Xuanqing Liu. Energy Deposition into the Ionosphere during a Solar Flare with Extreme-ultraviolet Late Phase. *Astrophys. J. Lett.*, 963(1):L8, March 2024. doi: 10.3847/2041-8213/ad250b.
- Kai Liu, Yuming Wang, Jie Zhang, Xin Cheng, Rui Liu, and Chenglong Shen. Extremely Large EUV Late Phase of Solar Flares. *Astrophys. J.*, 802(1):35, March 2015. doi: 10.1088/0004-637X/802/1/35.
- Fernando M. López, M. Hebe Cremades, Federico A. Nuevo, Laura A. Balmaceda, and Alberto M. Vásquez. Mass-Loss Evolution in the EUV Low Corona from SDO/AIA Data. *Sol. Phys.*, 292(1):6, January 2017. doi: 10.1007/s11207-016-1031-x.
- Wayne M. McRae and Neil R. Thomson. Solar flare induced ionospheric D-region enhancements from VLF phase and amplitude observations. *Journal of Atmospheric and Solar-Terrestrial Physics*, 66(1):77–87, January 2004. doi: 10.1016/j.jastp.2003.09.009.

- R. O. Milligan, P. T. Gallagher, M. Mathioudakis, D. S. Bloomfield, F. P. Keenan, and R. A. Schwartz. Rhesi and soho cds observations of explosive chromospheric evaporation. *Astrophys. J.*, 638(2):L117–L120, 2006. doi: 10.1086/499358.
- Ryan O. Milligan and Brian R. Dennis. Velocity Characteristics of Evaporated Plasma Using Hinode/EUV Imaging Spectrometer. *Astrophys. J.*, 699(2): 968–975, July 2009. doi: 10.1088/0004-637X/699/2/968.
- A. P. Mitra. *Ionospheric effects of solar flares*, volume 46. 1974. doi: 10.1007/978-94-010-2231-6.
- Werner M. Neupert. Comparison of Solar X-Ray Line Emission with Microwave Emission during Flares. *Astrophys. J. Lett.*, 153:L59, July 1968. doi: 10.1086/180220.
- Aisling N. O’Hare, Susanna Bekker, Laura A. Hayes, and Ryan O. Milligan. Quasi-Periodic Pulsations in Ionospheric TEC Synchronized With Solar Flare EUV Emission. *Journal of Geophysical Research (Space Physics)*, 130(4): e2024JA033493, April 2025. doi: 10.1029/2024JA033493.
- S. Orniq, A. M. Veronig, and K. Dissauer. Extreme ultraviolet late-phase flares as observed by EVE and AIA on board the Solar Dynamics Observatory. *Astron. Astrophys.*, 702:A49, October 2025. doi: 10.1051/0004-6361/202556242.
- P. Pant. Relation between VLF Phase Deviations and Solar X-Ray Fluxes during Solar Flares. *Astrophys. Space Sci.*, 209(2):297–306, November 1993. doi: 10.1007/BF00627449.
- W. Dean Pesnell, B. J. Thompson, and P. C. Chamberlin. The Solar Dynamics Observatory (SDO). *Sol. Phys.*, 275(1-2):3–15, January 2012. doi: 10.1007/s11207-011-9841-3.
- C. L. Raftery, P. T. Gallagher, R. O. Milligan, and J. A. Klimchuk. Multi-wavelength observations and modelling of a canonical solar flare. *Astron. Astrophys.*, 494(3):1127–1136, February 2009. doi: 10.1051/0004-6361:200810437.
- Jean-Pierre Raulin, Gérard Trottet, Matthieu Kretzschmar, Edith L. Macotela, Alessandra Pacini, Fernando C. P. Bertonni, and Ingolf E. Dammasch. Response of the low ionosphere to x-ray and lyman- α solar flare emissions. *Journal of Geophysical Research: Space Physics*, 118(1):570–575, 2013. doi: <https://doi.org/10.1029/2012JA017916>. URL <https://agupubs.onlinelibrary.wiley.com/doi/abs/10.1029/2012JA017916>.
- Jeffrey W. Reep, Harry P. Warren, Nicholas A. Crump, and Paulo J. A. Simões. Transition Region and Chromospheric Signatures of Impulsive Heating Events. II. Modeling. *Astrophys. J.*, 827(2):145, August 2016. doi: 10.3847/0004-637X/827/2/145.

- A. Savitzky and M. J. E. Golay. Smoothing and differentiation of data by simplified least squares procedures. *Analytical Chemistry*, 36:1627–1639, January 1964. doi: 10.1021/ac60214a047.
- P. J. A. Simoes, D. R. Graham, H. S. Hudson, and L. Fletcher. Preflare 131 Å hot onset observed by sdo/aia. *Solar Physics*, 290:3625–3640, 2015. doi: 10.1007/s11207-015-0770-5.
- Stanley C. Solomon and Liying Qian. Solar extreme-ultraviolet irradiance for general circulation models. *Journal of Geophysical Research (Space Physics)*, 110(A10):A10306, October 2005. doi: 10.1029/2005JA011160.
- Charles Spearman. The proof and measurement of association between two things. *The American Journal of Psychology*, 15(1):72–101, 1904. doi: 10.2307/1412159.
- P. A. Sturrock. Model of the High-Energy Phase of Solar Flares. *Nature*, 211(5050):695–697, August 1966. doi: 10.1038/211695a0.
- Xudong Sun, J. Todd Hoeksema, Yang Liu, Guillaume Aulanier, Yingna Su, Iain G. Hannah, and Rachel A. Hock. Hot Spine Loops and the Nature of a Late-phase Solar Flare. *Astrophys. J.*, 778(2):139, December 2013. doi: 10.1088/0004-637X/778/2/139.
- Cole A. Tamburri, Maria D. Kazachenko, and Adam F. Kowalski. The Relationships among Solar Flare Impulsiveness, Energy Release, and Ribbon Development. *Astrophys. J.*, 966(1):94, May 2024. doi: 10.3847/1538-4357/ad3047.
- The SunPy Community, Will T. Barnes, Monica G. Bobra, Steven D. Christe, Nabil Freij, Laura A. Hayes, Jack Ireland, Stuart Mumford, David Perez-Suarez, Daniel F. Ryan, Albert Y. Shih, Prateek Chanda, Kolja Glogowski, Russell Hewett, V. Keith Hughitt, Andrew Hill, Kaustubh Hiware, Andrew Inglis, Michael S. F. Kirk, Sudarshan Konge, James Paul Mason, Shane Anthony Maloney, Sophie A. Murray, Asish Panda, Jongyeob Park, Tiago M. D. Pereira, Kevin Reardon, Sabrina Savage, Brigitta M. Sipőcz, David Stansby, Yash Jain, Garrison Taylor, Tannmay Yadav, Rajul, and Trung Kien Dang. The sunpy project: Open source development and status of the version 1.0 core package. *The Astrophysical Journal*, 890:68–, 2020. doi: 10.3847/1538-4357/ab4f7a. URL <https://iopscience.iop.org/article/10.3847/1538-4357/ab4f7a>.
- Hui Tian, Peter R. Young, Katharine K. Reeves, Bin Chen, Wei Liu, and Sean McKillop. Temporal Evolution of Chromospheric Evaporation: Case Studies of the M1.1 Flare on 2014 September 6 and X1.6 Flare on 2014 September 10. *Astrophys. J.*, 811(2):139, October 2015. doi: 10.1088/0004-637X/811/2/139.
- Shin Toriumi and Haimin Wang. Flare-productive active regions. *Living Reviews in Solar Physics*, 16(1):3, December 2019. doi: 10.1007/s41116-019-0019-7.

- Kyoko Watanabe, Hidekatsu Jin, Shohei Nishimoto, Shinsuke Imada, Toshiki Kawai, Tomoko Kawate, Yuichi Otsuka, Atsuki Shinbori, Takuya Tsugawa, and Michi Nishioka. Model-based reproduction and validation of the total spectra of a solar flare and their impact on the global environment at the X9.3 event of September 6, 2017. *Earth, Planets and Space*, 73(1):96, December 2021. doi: 10.1186/s40623-021-01376-6.
- Edwin B. Wilson. Probable inference, the law of succession, and statistical inference. *Journal of the American Statistical Association*, 22(158):209–212, 1927. doi: 10.1080/01621459.1927.10502953. URL <https://www.tandfonline.com/doi/abs/10.1080/01621459.1927.10502953>.
- T. N. Woods, F. G. Eparvier, R. Hock, A. R. Jones, D. Woodraska, D. Judge, L. Didkovsky, J. Lean, J. Mariska, H. Warren, D. McMullin, P. Chamberlin, G. Berthiaume, S. Bailey, T. Fuller-Rowell, J. Sojka, W. K. Tobiska, and R. Viereck. Extreme Ultraviolet Variability Experiment (EVE) on the Solar Dynamics Observatory (SDO): Overview of Science Objectives, Instrument Design, Data Products, and Model Developments. *Sol. Phys.*, 275(1-2):115–143, January 2012. doi: 10.1007/s11207-009-9487-6.
- Thomas N. Woods. Extreme Ultraviolet Late-Phase Flares: Before and During the Solar Dynamics Observatory Mission. *Sol. Phys.*, 289(9):3391–3401, September 2014. doi: 10.1007/s11207-014-0483-0.
- Thomas N. Woods, Rachel Hock, Frank Eparvier, Andrew R. Jones, Phillip C. Chamberlin, James A. Klimchuk, Leonid Didkovsky, Darrell Judge, John Mariska, Harry Warren, Carolus J. Schrijver, David F. Webb, Scott Bailey, and W. Kent Tobiska. New Solar Extreme-ultraviolet Irradiance Observations during Flares. *Astrophys. J.*, 739(2):59, October 2011. doi: 10.1088/0004-637X/739/2/59.
- D. H. Zhang, X. H. Mo, L. Cai, W. Zhang, M. Feng, Y. Q. Hao, and Z. Xiao. Impact factor for the ionospheric total electron content response to solar flare irradiation. *Journal of Geophysical Research (Space Physics)*, 116(A4):A04311, April 2011. doi: 10.1029/2010JA016089.
- Y. Zhong, Y. Dai, and M. D. Ding. Extreme-ultraviolet Late Phase in Homologous Solar Flares from a Complex Active Region. *Astrophys. J.*, 916(1):37, July 2021. doi: 10.3847/1538-4357/ac0430.
- Zhenjun Zhou, Xin Cheng, Lijuan Liu, Yu Dai, Yuming Wang, and Jun Cui. Extreme-ultraviolet Late Phase Caused by Magnetic Reconnection over Quadrupolar Magnetic Configuration in a Solar Flare. *Astrophys. J.*, 878(1):46, June 2019. doi: 10.3847/1538-4357/ab1d5c.